Nonparametric distributions of tensor-valued Lorentzian diffusion spectra for model-free data inversion in multidimensional diffusion MRI

N.B. When citing this work, cite the original published paper.

(article starts on next page)

Nonparametric distributions of tensor-valued Lorentzian diffusion spectra for model-free data inversion in multidimensional diffusion MRI

Omar Narvaez [iD] ; Maxime Yon; Hong Jiang; Diana Bernin [iD] ; Eva Forssell-Aronsson [iD] ; Alejandra Sierra [iD] ; Daniel Topgaard [✉] [iD]

View Online

Export Citation

The Journal of Chemical Physics

Special Topic: Molecular Dynamics, Methods and Applications 60 Years after Rahman

Submit Today

AIP Publishing

AIP Publishing

Nonparametric distributions of tensor-valued Lorentzian diffusion spectra for model-free data inversion in multidimensional diffusion MRI

View Online   Export Citation   CrossMark

Omar Narvaez,[1] (ID) Maxime Yon,[2] Hong Jiang,[2] Diana Bernin,[3] (ID) Eva Forsell-Aronsson,[4,5,6] (ID)
Alejandra Sierra,[1] (ID) and Daniel Topgaard[2,a)] (ID)

AFFILIATIONS

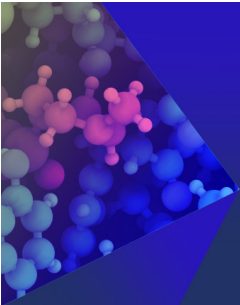[1] A.I.Virtanen Institute for Molecular Sciences, University of Eastern Finland, Kuopio, Finland
[2] Department of Chemistry, Lund University, Lund, Sweden
[3] Department of Chemistry and Chemical Engineering, Chalmers University of Technology, Gothenburg, Sweden
[4] Department of Medical Radiation Sciences, University of Gothenburg, Gothenburg, Sweden
[5] Medical Physics and Biomedical Engineering, Sahlgrenska University Hospital, Gothenburg, Sweden
[6] Sahlgrenska Center for Cancer Research, Sahlgrenska Academy at the University of Gothenburg, Gothenburg, Sweden

[a)] Author to whom correspondence should be addressed: daniel.topgaard@fkem1.lu.se

ABSTRACT

Magnetic resonance imaging (MRI) is the method of choice for noninvasive studies of micrometer-scale structures in biological tissues via their effects on the time- and frequency-dependent (restricted) and anisotropic self-diffusion of water. While new designs of time-dependent magnetic field gradient waveforms have enabled disambiguation between different aspects of translational motion that are convolved in traditional MRI methods relying on single pairs of field gradient pulses, data analysis for complex heterogeneous materials remains a challenge. Here, we propose and demonstrate nonparametric distributions of tensor-valued Lorentzian diffusion spectra, or "$\mathbf{D}(\omega)$ distributions," as a general representation with sufficient flexibility to describe the MRI signal response from a wide range of model systems and biological tissues investigated with modulated gradient waveforms separating and correlating the effects of restricted and anisotropic diffusion.

I. INTRODUCTION

Nuclear magnetic resonance (NMR) and magnetic resonance imaging (MRI) offer noninvasive characterization of cellular-level structures in intact biological tissues by employing time-dependent magnetic field gradients to monitor the micrometer-scale translational motion of water molecules[1,2] and, by inference, their interactions with cell membranes and macromolecules.[3,4] While the use of diffusion MRI is, in current clinical practice, limited to rather basic measurements of diffusion-weighted images and apparent diffusion coefficients[5] to detect and grade ischemic stroke[6] and tumors,[7] there is a recent trend of applying increasingly advanced motion-encoding gradients to isolate specific aspects of translational motion, such as anisotropy,[8] restriction,[9] flow,[10] and exchange.[11] Despite the developments of specific encoding strategies and

numerous examples of promising applications in clinical research,[12] data analysis and interpretation remain challenging—in particular for heterogeneous tissues where each imaging voxel contains multiple water populations with distinct diffusion properties.[13,14]

Translational motion of an ensemble of particles can be described in the time domain, with mean-square displacements,[15] apparent diffusivities,[16] and velocity autocorrelation functions,[17] or in the frequency domain with tensor-valued diffusion spectra $\mathbf{D}(\omega)$ being the Fourier transformation of the latter.[18,19] The relations between the time- and frequency-domain descriptions are explained in detail in text books[1,2] and reviews.[20–22] Although it is challenging to decide if time- or frequency-domain analysis is "best" suited for a given application, numerous recent papers indicate that the frequency-domain approach may be preferred for *in vivo* human studies.[23–29]

While the ω-dependence of $\mathbf{D}(\omega)$ can be approximated as Lorentzian, corresponding to an exponential velocity autocorrelation function,[17,30] more accurate expressions have been derived for simple pore shapes, such as parallel planes, cylinders, and spheres,[31] as well as random permeable barriers.[32] The latter model implies structural disorder rather than a particular geometric shape and has been applied for analysis of *in vivo* human brain data in several recent publications.[24,27,33,34] The ω-dependence of the elements of $\mathbf{D}(\omega)$ may be mapped out in detail by applying modulated gradients $\mathbf{g}(t)$, yielding tensor-valued encoding spectra $\mathbf{b}(\omega)$ with spectral power focused on selected sets of tensor elements and values of ω.[22] The experimentally accessible range of ω is determined by the performance of the gradient hardware and, in practice, is often limited to the rather narrow windows ~10–100 Hz for human[26,27] and ~10–1000 Hz for small-specimen[35] MRI systems, thus making it difficult to distinguish between different candidate models from the observed ω-dependence alone.

For measurements performed with a fixed ω-range, data analysis is often based on an ω-independent diffusion tensor $\mathbf{D}$ corresponding to a section of the full spectrum $\mathbf{D}(\omega)$. Here, the relevant acquisition variable is the encoding tensor $\mathbf{b}$,[36] given by the integral of $\mathbf{b}(\omega)$ over all ω,[37] and conveniently parameterized by its magnitude b, anisotropy b_Δ, asymmetry b_η, and orientation (Ψ, Θ, Φ).[38–40] The presence of multiple water populations in heterogeneous tissues is frequently described in terms of discrete[41–46] or continuous[47–51] diffusion tensor distributions (DTDs). While conventional diffusion MRI with motion encoding by a single pair of gradient pulses[52] is constrained to the acquisition parameters b and (Θ, Φ), colloquially known as the "b-value" and "b-vector," more sophisticated gradient modulation schemes[53,54] give access to the tensor "shape" parameters b_Δ and b_η,[38–40] which enable Monte Carlo data inversion into nonparametric DTDs[57–60] with limited contributions from spurious components that occur when the shape dimensions are not sufficiently explored.[61,62]

We have recently introduced a family of "double-rotation" gradient waveforms for the exploration of both the spectral and tensorial aspects of $\mathbf{b}(\omega)$.[37,63] Special cases of these waveforms include the classical single pair of gradient pulses sensitive to anisotropy, restriction, and flow;[52] two pulse pairs for flow compensation;[64] trains of pulse pairs[19] or cosine-modulated oscillating gradients to probe diffusion at a well-defined frequency;[65] circularly polarized oscillating gradients to increase the b-value for a given frequency and maximum gradient strength;[66] magic-angle spinning of the q-vector[67] to minimize the influence of anisotropy;[54] and variable-angle spinning of the q-vector[68] for probing the tensor "shape" dimensions,[55,56] thereby allowing convenient collection of rich datasets incorporating subsets that can be identified as diffusion tensor imaging (low b-values, multiple directions, constant spectral content, and linear b-tensor shape),[69] diffusional kurtosis imaging (high b-values, multiple directions, constant spectral content, and linear b-tensor shape),[70] diffusion dispersion imaging (low b-values, few directions, multiple encoding frequencies, and linear b-tensor shape),[24] and microscopic anisotropy imaging (high b-values, multiple directions, limited variation of spectral content, and multiple b-tensor shapes).[71,72]

With the availability of rich and multifaceted data comes the challenge of data analysis having sufficient flexibility to incorporate all the acquisition variables (b-values, directions, spectral contents,

and b-tensor shapes) of the methods mentioned above. In particular, previous versions of DTD analysis[41–51,57–60] neglect the effects of time- and frequency-dependent diffusivities. When extending the DTD approach to restricted diffusion, one option is confinement tensor distributions,[73] which are ideally suited for time-domain analysis.[74] Our focus on the frequency domain, however, makes distributions of frequency-dependent diffusion tensors, or "$\mathbf{D}(\omega)$ distributions," a more natural choice. Expanding on and partially incorporating a preprint with detailed description of the theoretical background and formal analogy with NMR relaxation dispersion of biological macromolecules,[75] we here demonstrate the ability of our proposed method to reproduce the synthetic data generated by the random permeable barrier model,[32] resolve and quantify restriction and anisotropy for multiple components in well-defined phantoms, and generate maps of parameters correlating restriction and anisotropy in *ex vivo* rat brain and excised tissue from a xenograft model of neuroblastoma.[76] Encouraged by the recent profusion of *in vivo* human studies using nearly identical MRI pulse sequences to explore either the spectral[23–29] or tensorial[60,77–81] aspects of the diffusion encoding, we envision that our unification of the traditionally separate strategies into a common analysis framework will catalyze the design of more informative and time-efficient data acquisition protocols for clinical research studies of tissue microstructure in health and disease.

II. THEORETICAL BACKGROUND

A. Tensor-valued diffusion spectra for some special cases

Consider an ensemble of spins with individual velocities $\mathbf{v}(t)$, which can be separated into the ensemble mean $\langle\mathbf{v}\rangle$ and fluctuating part $\mathbf{u}(t)$, according to

$$\mathbf{u}(t) = \mathbf{v}(t) - \langle\mathbf{v}\rangle. \quad (1)$$

The tensor-valued diffusion spectrum $\mathbf{D}(\omega)$ is defined from the velocity correlation function $\langle\mathbf{u}(t)\mathbf{u}(t')^\mathrm{T}\rangle$, where T denotes a matrix transpose, via the Fourier transformation,[1,2]

$$\mathbf{D}(\omega) = \frac{1}{2}\int_{-\infty}^{\infty}\langle\mathbf{u}(t)\mathbf{u}(t')^\mathrm{T}\rangle\exp\left(i\omega(t'-t)\right)\mathrm{d}(t'-t), \quad (2)$$

which can be expanded as

$$\mathbf{D}(\omega) = \mathbf{R}(\psi,\theta,\phi)\begin{pmatrix} D_{XX}(\omega) & 0 & 0 \\ 0 & D_{YY}(\omega) & 0 \\ 0 & 0 & D_{ZZ}(\omega) \end{pmatrix}\mathbf{R}^{-1}(\psi,\theta,\phi),$$
$$(3)$$

where $\mathbf{R}(\psi, \theta, \phi)$ is a rotation matrix; (ψ, θ, ϕ) are Euler angles; and $D_{XX}(\omega)$, $D_{YY}(\omega)$, and $D_{ZZ}(\omega)$ are the diagonal diffusion spectra in the principal axis system.

Approximating the velocity correlation with one positive exponential with decay rate Γ_0 for the transition from the ballistic to diffusive regime[17] and a negative exponential with decay rate Γ_1 for interactions with the pore walls[30] leads to a bi-Lorentzian expression,

$$D(\omega) = \frac{D_0}{1 + \omega^2/\Gamma_0^2} - \frac{D_0 - D_\infty}{1 + \omega^2/\Gamma_1^2}, \quad (4)$$

where $D(\omega)$ symbolizes any or all of $D_{XX}(\omega)$, $D_{YY}(\omega)$, and $D_{ZZ}(\omega)$; D_0 is the diffusivity of the pure liquid; and D_∞ is the long-time diffusivity of the liquid in the porous matrix. For water and other low molecular weight liquids, the value of Γ_0 is many orders of magnitude larger than the maximum value of ω accessible with NMR methods, and the first term in Eq. (4) can be replaced with D_0.

The exact expression for planar, cylindrical, and spherical pores can be written as[31,82]

$$D(\omega) = D_0 - \sum_{k=1}^{\infty} w_k \frac{D_0 - D_\infty}{1 + \omega^2/\Gamma_k^2}, \tag{5}$$

where $D_{ZZ}(\omega) = D(\omega)$ and $D_{XX}(\omega) = D_{YY}(\omega) = D_0$ for the planar, $D_{ZZ}(\omega) = D_0$ and $D_{XX}(\omega) = D_{YY}(\omega) = D(\omega)$ for the cylindrical, and $D_{XX}(\omega) = D_{YY}(\omega) = D_{ZZ}(\omega) = D(\omega)$ for the spherical model. The multi-Lorentzian transition in the second term of Eq. (5) is determined by the weights w_k and rates Γ_k, given by

$$w_k = \frac{2}{\zeta_k^2 + 1 - d} \tag{6}$$

and

$$\Gamma_k = \frac{\zeta_k^2 D_0}{r^2}, \tag{7}$$

where $d = 1$, 2, and 3 for the planar, cylindrical, and spherical cases, respectively; r is the pore radius; and ζ_k is the kth solution of

$$\zeta J_{d/2-1}(\zeta) - (d-1)J_{d/2}(\zeta) = 0, \tag{8}$$

and J_ν is the νth order Bessel function of the first kind.

The random permeable barrier model developed by Novikov et al.[83] can be expressed as

$$D(\omega) = \frac{D_0}{\frac{D_0}{D_\infty} + 2z_\omega(1 - z_\omega)\left[\sqrt{1 + \frac{D_0/D_\infty - 1}{(1 - z_\omega)^2}} - 1\right]}, \tag{9}$$

where

$$z_\omega = i\sqrt{i\omega/\Gamma}, \tag{10}$$

and Γ is the characteristic transition rate. The parameters D_∞ and Γ are related to the permeability and average spacing between the barriers.

Figure 1 shows the diffusion spectra calculated with Eqs. (4), (5), and (9) using parameters selected to produce similar isotropic diffusivity $D_{\text{iso}}(\omega)$, defined as

$$D_{\text{iso}}(\omega) = \frac{1}{3}\text{trace}\{\mathbf{D}(\omega)\}. \tag{11}$$

In the diffusion NMR and MRI literature, the term "Gaussian diffusion" refers to a mean-square displacement scaling linearly with time, which corresponds to diffusivities independent of time and frequency. Thus, Fig. 1 shows low- and high-ω limits with Gaussian diffusion separated by a transition region with restricted diffusion characterized by time- and frequency-dependent diffusivities. On the scale shown in Fig. 1, the Lorentzian, planar,
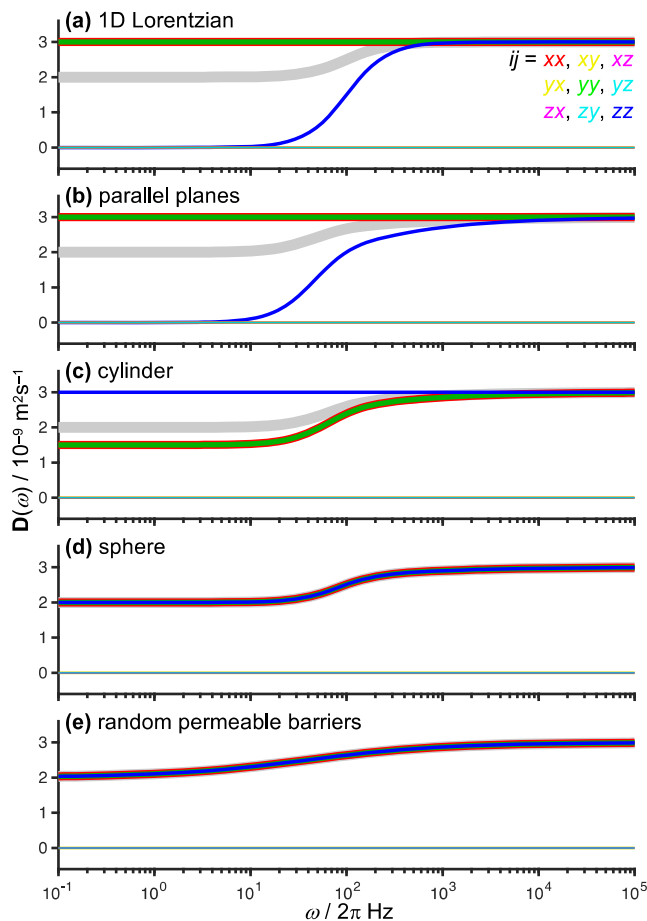

FIG. 1. Theoretical tensor-valued diffusion spectra $\mathbf{D}(\omega)$ for selected special cases. The tensor elements are color coded according to the legend (top right), and the isotropic diffusivity $D_{\text{iso}}(\omega)$, see Eq. (11), is shown in gray. All the cases have $D_{\text{iso}}(0) = 2 \times 10^{-9}$ m^{2}s^{-1}, transition from low- to high-ω plateau centered on ~100 Hz, bulk diffusivity $D_0 = 3 \times 10^{-9}$ m^{2}s^{-1}, and Euler angles $(\psi, \theta, \phi) = (0, 0, 0)$. (a) 1D Lorentzian with $D_{XX}(\omega) = D_{YY}(\omega) = D_0$ and $D_{ZZ}(\omega)$ is given by Eq. (4) with rate $\Gamma_1 = 2\pi \times 100$ s^{-1}. (b) Parallel planes with $D_{XX}(\omega) = D_{YY}(\omega) = D_0$ and $D_{ZZ}(\omega)$ given by Eq. (5) with $d = 1$ and $r = 5$ μm. (c) Cylinder with $D_{ZZ}(\omega) = D_0$ and $D_{XX}(\omega) = D_{YY}(\omega)$ given by Eq. (5) with $d = 2$ and $r = 5$ μm. (d) Sphere with $D_{XX}(\omega) = D_{YY}(\omega) = D_{ZZ}(\omega)$ given by Eq. (5) with $d = 3$ and $r = 5$ μm. (e) Random permeable barrier model with $D_{XX}(\omega) = D_{YY}(\omega) = D_{ZZ}(\omega)$ given by Eq. (9) with $\Gamma = 100$ s^{-1}.

cylindrical, and spherical cases in panels (a)–(d) yield $D_{\text{iso}}(\omega)$ that are nearly indistinguishable, with a transition region that extends over more than two orders of magnitude of ω. Closer inspection reveals that the transition gets increasingly broader from the top to the bottom of the figure, with the random permeable barrier model in panel (e) being distinctly smoother than the others. As mentioned in the introduction, clinical and preclinical MRI equipment offer one and two orders of magnitude of experimentally accessible ω-ranges, respectively, thus making it challenging to estimate both the low- and high-ω plateaus and the details of the transition.

B. Frequency-domain analysis of motion with modulated gradient NMR

Within the Gaussian phase distribution approximation (not to be confused with the term Gaussian diffusion),[18,22,31,84] the signal $S[\mathbf{q}_v, \mathbf{b}(\omega)]$ is given by

$$S[\mathbf{q}_v, \mathbf{b}(\omega)] = S_0 \exp\left(i\mathbf{q}_v \cdot \langle\mathbf{v}\rangle - \int_{-\infty}^{\infty} \mathbf{b}(\omega) : \mathbf{D}(\omega)\,d\omega\right), \quad (12)$$

where the motion encoding properties are summarized by the velocity encoding vector $\mathbf{q}_v$ and the tensor-valued diffusion encoding spectrum $\mathbf{b}(\omega)$, which are obtained from the time-dependent magnetic field gradient vector $\mathbf{g}(t)$ via

$$\mathbf{q}(t) = \gamma \int_0^t \mathbf{g}(t')\,dt', \quad (13)$$

$$\mathbf{q}_v = \int_0^\tau \mathbf{q}(t)\,dt, \quad (14)$$

$$\mathbf{q}(\omega) = \int_0^\tau \mathbf{q}(t)\exp(i\omega t)\,dt, \quad (15)$$

and

$$\mathbf{b}(\omega) = \frac{1}{2\pi}\mathbf{q}(\omega)\mathbf{q}(-\omega)^\mathrm{T}. \quad (16)$$

In the equations above, S_0 is the reference signal at $\mathbf{g}(t) = 0$, the colon denotes a generalized scalar product,[36] γ is the gyromagnetic ratio of the studied atomic nucleus, τ is the overall duration of the motion-encoding gradients, $\mathbf{q}(t)$ is the time-dependent dephasing vector subject to the echo condition $\mathbf{q}(\tau) = 0$, and $\mathbf{q}(\omega)$ is the frequency-domain spectrum of $\mathbf{q}(t)$.

While the full ω-dependent and tensorial representation of $\mathbf{b}(\omega)$ is used in our data processing, we find it instructive to summarize its most important aspects using the magnitude b,[36,85] "effective"[86] or "centroid"[24] frequency ω_{cent}, and the anisotropy b_Δ and asymmetry b_η quantifying the tensor "shape" using conventions from the field of solid-state NMR.[38–40] These variables are defined through the equations,

$$\mathbf{b} = \int_{-\infty}^{\infty} \mathbf{b}(\omega)\,d\omega, \quad (17)$$

$$b(\omega) = \text{trace}\{\mathbf{b}(\omega)\}, \quad (18)$$

$$b = \text{trace}\{\mathbf{b}\} = \int_{-\infty}^{\infty} b(\omega)\,d\omega, \quad (19)$$

$$\omega_{\text{cent}} = \frac{1}{b}\int_{-\infty}^{\infty} |\omega|b(\omega)\,d\omega, \quad (20)$$

$$b_\Delta = \frac{1}{b}\left(b_{ZZ} - \frac{b_{YY} + b_{XX}}{2}\right), \quad (21)$$

and

$$b_\eta = \frac{3}{2}\frac{b_{YY} - b_{XX}}{bb_\Delta}. \quad (22)$$

In Eq. (17), $\mathbf{b}$ is the conventional (ω-independent) b matrix[36] with eigenvectors given by the three Euler angles (Ψ, Θ, and Φ). In Eqs. (21) and (22), b_{XX}, b_{YY}, and b_{ZZ} are the eigenvalues of $\mathbf{b}$ ordered according to the Haeberlen convention $|b_{ZZ} - b/3| > |b_{XX} - b/3| > |b_{YY} - b/3|$.[87]

Conventional diffusion MRI is constrained to the acquisition variables b and (Θ, Φ) with $b_\Delta = 1$, $b_\eta = 0$, and constant ω_{cent}. Oscillating gradients allow exploration of the ω_{cent} dimension,[21] and tensor-valued encoding brings in variation of b_Δ and b_η as well as the third Euler angle Ψ.[40] All these variables are accessible with the double-rotation gradient waveforms generated according to the recipe described in detail by Jiang et al.[37] and summarized in the following.

1. Select a one-dimensional waveform $g_{1D}(t)$ from a dephasing lobe with quarter-sine ramp up of duration ε_{up} and half-cosine ramp down of duration $\varepsilon_{\text{down}}$, as well as a rephasing lobe obtained by inversion and time-reversal of the dephasing one.
2. Calculate the magnitude of a rotating gradient waveform $g_{\text{rot}}(t)$ by

$$g_{\text{rot}}(t) = \frac{\Delta\psi_2 q^3(t)}{\gamma b}, \quad (23)$$

where

$$q(t) = \gamma \int_0^t g_{1D}(t')\,dt' \quad (24)$$

and

$$\psi_2(t) = \frac{\Delta\psi_2}{b}\int_0^t q^2(t')\,dt'. \quad (25)$$

In Eq. (25), $\Delta\psi_2$ is an overall angle of rotation during the waveform duration τ.

3. Assemble the scalar $g_{1D}(t)$ and $g_{\text{rot}}(t)$ into a vectorial double-rotation waveform $\mathbf{g}_{\text{DOR}}(t)$, according to

$$\mathbf{g}_{\text{DOR}}(t) = g_{1D}(t)\begin{pmatrix} a_+ \cos\psi_+(t) + a_- \cos\psi_-(t) + a_2 \cos\psi_2(t) \\ a_+ \sin\psi_+(t) - a_- \sin\psi_-(t) + a_2 \sin\psi_2(t) \\ a_0 - a_1 \cos\psi_1(t) \end{pmatrix}$$
$$+ g_{\text{rot}}(t)\begin{pmatrix} -(n+1)a_+ \sin\psi_+(t) - (n-1)a_- \sin\psi_-(t) - a_2 \sin\psi_2(t) \\ (n+1)a_+ \cos\psi_+(t) - (n-1)a_- \cos\psi_-(t) + a_2 \cos\psi_2(t) \\ na_1 \sin\psi_1(t) \end{pmatrix}, \quad (26)$$

where

$$\psi_1(t) = n\psi_2(t),$$
$$\psi_\pm(t) = (n \pm 1)\psi_2(t), \tag{27}$$

and

$$a_0 = \cos\zeta_1 \cos\zeta_2,$$
$$a_1 = \sin\zeta_1 \sin\zeta_2,$$
$$a_2 = \cos\zeta_1 \sin\zeta_2, \tag{28}$$
$$a_\pm = \sin\zeta_1 \frac{\cos\zeta_2 \pm 1}{2}.$$

In Eq. (28), $\zeta_1 = 90°$ and $\zeta_2 = -54.7°$ for positive integer values of the double-rotation ratio n and $\zeta_1 = 54.7°$ and $\zeta_2 = 0°$ for $n = 0$.

4.   Scale and rotate the components of $\mathbf{g}_{DOR}(t)$ by

$$\mathbf{g}(t) = \mathbf{R}_z(\Phi)\mathbf{R}_y(\Theta)\mathbf{R}_z(\Psi)\begin{bmatrix} g_{DOR,X}(t)\sqrt{1-b_\Delta(1+b_\eta)} \\ g_{DOR,Y}(t)\sqrt{1-b_\Delta(1-b_\eta)} \\ g_{DOR,Z}(t)\sqrt{1+2b_\Delta} \end{bmatrix}. \tag{29}$$

Figure 2 shows an example of a double-rotation gradient waveform to investigate the spectral and tensorial aspects of $\mathbf{D}(\omega)$, which are manifested as unequal diagonal elements and finite off-diagonal elements in the $\omega = 0$ regime in panel (a). The waveform yields an encoding spectrum $\mathbf{b}(\omega)$, which determines the signal attenuation via the integral of the generalized scalar product $\mathbf{b}(\omega) : \mathbf{D}(\omega)$ over ω according to Eq. (12). The encoding power is focused on a narrow band in the approximate range of ω from $n\Delta\psi_2/\tau$ to $(n+1)\Delta\psi_2/\tau$,[37] which at constant $\Delta\psi_2$ and τ is conveniently shifted by varying n. Correspondingly, the values of b_Δ and b_η determine the balance between the eigenvalues of $\mathbf{b}(\omega)$ and the sensitivity of the signal to anisotropy of $\mathbf{D}(\omega)$. A rather complete investigation of restriction and anisotropy could thus be achieved by performing measurements as a function of n, b_Δ, and b_η, in addition to the variables b and (Θ, Φ) of conventional diffusion MRI.

C. Multiple sub-ensembles and the axisymmetric Lorentzian approximation

For a heterogeneous system comprising multiple sub-ensembles i with weights w_i, Eq. (12) can be generalized to

$$S[\mathbf{q}_v, \mathbf{b}(\omega)] = \sum_i w_i \exp\left(i\mathbf{q}_v \cdot \langle\mathbf{v}_i\rangle - \int_{-\infty}^{\infty} \mathbf{b}(\omega) : \mathbf{D}_i(\omega)d\omega\right). \tag{30}$$

The popular diffusion tensor distribution[41–51,58–60] approach to account for intravoxel heterogeneity of biological tissues relies on the assumptions $\langle\mathbf{v}_i\rangle = 0$ and $\mathbf{D}_i(\omega)$ being constant within the range of ω where $\mathbf{b}(\omega)$ is non-zero. With these assumptions, Eq. (30) reduces to the more familiar expression,

$$S(\mathbf{b}) = \sum_i w_i \exp(-\mathbf{b} : \mathbf{D}_i). \tag{31}$$

For analysis of the experimental data in this paper, we do not make these conventional assumptions but instead use gradient
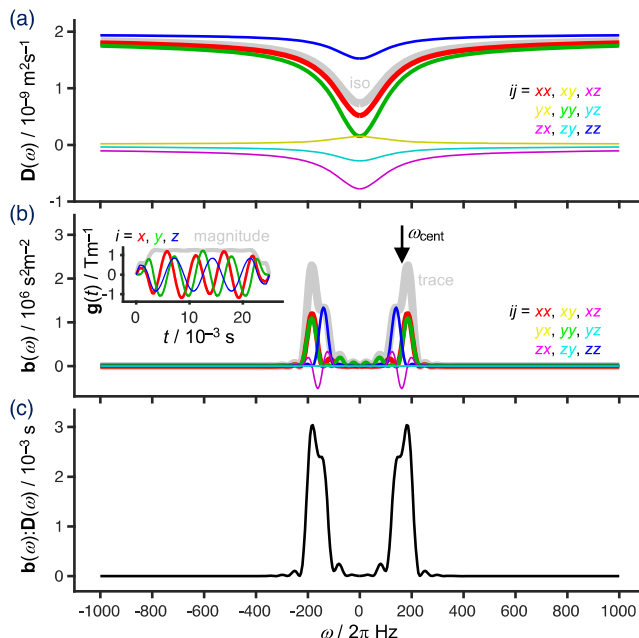

FIG. 2. Frequency-domain analysis of restricted and anisotropic diffusion with modulated gradients. (a) Tensor-valued diffusion spectrum $\mathbf{D}(\omega)$ for a liquid confined in a cylindrical compartment calculated with Eqs. (3) and (5) using bulk diffusivity $D_0 = 2 \times 10^{-9}$ m^{2}s^{-1}, long-time diffusivity $D_\infty = 0.1 \times 10^{-9}$ m^{2}s^{-1}, radius $r = 3$ μm, and Euler angles $(\psi, \theta, \phi) = (0°, -30°, 20°)$. Color coding of the elements $D_{ij}(\omega)$ is given in the legend to the right and the isotropic diffusivity $D_{iso}(\omega)$, see Eq. (11), is shown in gray. (b) Tensor-valued encoding spectrum $\mathbf{b}(\omega)$ obtained via Eqs. (13), (15), and (16) from the double-rotation gradient $\mathbf{g}(t)$, shown in the inset, calculated with Eqs. (23)–(29) using $\tau = 25$ ms, $\varepsilon_{up} = 0.03\tau$, $\varepsilon_{down} = 0.12\tau$, $\Delta\psi_2 = 2\pi$, $n = 3$, $b_\Delta = b_\eta = 0$, and $(\Psi, \Theta, \Phi) = (0, 0, 0)$. The arrow points out the centroid frequency ω_{cent} defined from the trace of $\mathbf{b}(\omega)$ in Eq. (20). (c) Generalized scalar product $\mathbf{b}(\omega) : \mathbf{D}(\omega)$, which, upon integration over ω, gives the signal attenuation factor according to Eq. (12).

waveforms for which $\mathbf{q}_v = 0$ and enable inversion of Eq. (30) by making an educated guess that each sub-ensemble is described with an axisymmetric tensor,

$$\mathbf{D}_i(\omega) = \mathbf{R}(\theta_i, \phi_i)\begin{pmatrix} D_{\perp,i}(\omega) & 0 & 0 \\ 0 & D_{\perp,i}(\omega) & 0 \\ 0 & 0 & D_{\parallel,i}(\omega) \end{pmatrix}\mathbf{R}^{-1}(\theta_i, \phi_i), \tag{32}$$

where the parallel and perpendicular eigenvalues, $D_{\parallel,i}(\omega)$ and $D_{\perp,i}(\omega)$, are given by Lorentzian transitions, at the frequencies $\Gamma_{\parallel,i}$ and $\Gamma_{\perp,i}$, between the zero-ω values, $D_{\parallel,i}$ and $D_{\perp,i}$, and the common high-ω plateau, $D_{0,i}$, according to

$$D_{\parallel,i}(\omega) = D_{0,i} - \frac{D_{0,i} - D_{\parallel,i}}{1 + \omega^2/\Gamma_{\parallel,i}^2} \tag{33}$$

and

$$D_{\perp,i}(\omega) = D_{0,i} - \frac{D_{0,i} - D_{\perp,i}}{1 + \omega^2/\Gamma_{\perp,i}^2}. \tag{34}$$

We emphasize that the axisymmetric Lorentzian approximation is made for mathematical convenience and does not imply

any specific compartment geometry or model as the expressions in Eqs. (5) and (9). In the following, we will demonstrate its utility by reproducing data synthesized with the random permeable barrier model and providing meaningful analysis of experimental data with well-defined restricted and anisotropic diffusion.

D. Data inversion and visualization

With the axisymmetric Lorentzian approximation, each discrete component in the $\mathbf{D}(\omega)$ distribution is described with its weight w and the parameter set $[D_\parallel, D_\perp, \theta, \phi, D_0, \Gamma_\parallel, \Gamma_\perp]$. Data inversion can then be performed by straightforward extension of the Monte Carlo method[88] that has previously been applied for various diffusion and relaxation correlation measurements, including $[D_\parallel, D_\perp]$,[57] $[D_\parallel, D_\perp, \theta, \phi]$,[58–60] $[D_\parallel, D_\perp, \theta, \phi, R_2]$,[89,90] $[D_\parallel, D_\perp, \theta, \phi, R_1]$,[91] and $[D_\parallel, D_\perp, \theta, \phi, R_1, R_2]$,[61,92] where R_1 and R_2 are the longitudinal and transverse relaxation rates. The Monte Carlo inversion yields ensembles of solutions that are all consistent with the data but where the individual realizations of the ensemble are "overfits," containing spurious details consistent with, but not necessarily required by, the acquired data. From the solution ensemble, it is possible to derive coarse-grained metrics, such as means and (co)variances over relevant dimensions, which are determined with higher precision quantifiable by bootstrapping.[58,88,93]

The discrepancy between the broad transition widths shown in Fig. 1 and the narrow ω-ranges experimentally accessible makes it nearly impossible to determine the low-ω plateaus $D_\parallel$ and $D_\perp$ simultaneously as the high-ω plateau D_0, thus making the primary analysis space $[D_\parallel, D_\perp, \theta, \phi, D_0, \Gamma_\parallel, \Gamma_\perp]$ unsuitable for extracting quantitative metrics. As a workaround, we propose evaluating the $\mathbf{D}(\omega)$ distributions at selected values of ω within the narrow range actually probed by the gradient waveforms, giving $[D_\parallel(\omega), D_\perp(\omega), \theta, \phi]$ via Eqs. (33) and (34). Following common practice in the field,[69] we also visualize the data by projecting the eigenvalues onto dimensions cleanly separating the magnitude and anisotropy of the diffusion tensors, in our case expressed in terms of the isotropic diffusivity $D_{\text{iso}}(\omega)$, via Eq. (11), and squared normalized anisotropy $D_\Delta^2(\omega)$, defined as[38,58,94]

$$D_\Delta^2(\omega) = \frac{\left[D_\parallel(\omega) - D_\perp(\omega)\right]^2}{\left[D_\parallel(\omega) + 2D_\perp(\omega)\right]^2}. \qquad (35)$$

The distributions can then be visualized as contour plots in the 2D D_{iso}-D_Δ^2 projections as well as condensed into (bin-resolved) signal fractions $f_{\text{bin}n}$, means $\text{E}_{\text{bin}n}[X]$, variances $\text{V}_{\text{bin}n}[X]$, and covariances $\text{C}_{\text{bin}n}[X, Y]$ suitable for generating parameter maps.[58] These metrics are given by

$$f_{\text{bin}n} = \frac{1}{S_0} \sum_{i \in \text{bin}n} w_i, \qquad (36)$$

$$\text{E}_{\text{bin}n}[X] = \frac{1}{S_0 f_{\text{bin}n}} \sum_{i \in \text{bin}n} w_i X_i, \qquad (37)$$

$$\text{V}_{\text{bin}n}[X] = \frac{1}{S_0 f_{\text{bin}n}} \sum_{i \in \text{bin}n} w_i (X_i - \text{E}[X])^2, \qquad (38)$$

and

$$\text{C}_{\text{bin}n}[X, Y] = \frac{1}{S_0 f_{\text{bin}n}} \sum_{i \in \text{bin}n} w_i (X_i - \text{E}[X])(Y_i - \text{E}[Y]), \qquad (39)$$

where X and Y symbolize $D_{\text{iso}}(\omega)$ or $D_\Delta^2(\omega)$,

$$S_0 = \sum_i w_i \qquad (40)$$

is the total signal extrapolated to $b = 0$, and the sums in Eqs. (36)–(39) are taken over components i belonging to the nth bin in the 2D D_{iso}-D_Δ^2 space.[58] Following previous oscillating gradient studies,[24,95,96] the effects of restriction are quantified as a finite difference approximation of the rates of change of these metrics within the investigated frequency window from ω_{min} to ω_{max}, for instance,

$$\Delta_{\omega/2\pi} \text{E}_{\text{bin}n}[D_{\text{iso}}] = \frac{\text{E}_{\text{bin}n}[D_{\text{iso}}(\omega_{\text{max}})] - \text{E}_{\text{bin}n}[D_{\text{iso}}(\omega_{\text{min}})]}{(\omega_{\text{max}} - \omega_{\text{min}})/2\pi}. \qquad (41)$$

To avoid clutter, the subscript "bin$n$" is omitted for the statistical descriptors $\text{E}[X]$, $\text{V}[X]$, and $\text{C}[X,Y]$ in the remainder of this paper.

Several of the metrics defined in Eqs. (36)–(41) are equivalent to well-known parameters from the literature:[58] $\text{E}[D_{\text{iso}}]$ is identical to the mean diffusivity; $\text{E}[D_\Delta^2]$ contains the same information as the microscopic anisotropy index,[97] microscopic fractional anisotropy,[71,98] and fractional eccentricity;[99] $\text{V}[D_{\text{iso}}]$ has appeared under numerous symbols, such as μ_2^{iso},[71] V_I,[72] and V_{MD};[56] and $\Delta_{\omega/2\pi}\text{E}[D_{\text{iso}}]$ is more commonly known as $\Delta_f\text{ADC}$[95] or the diffusion dispersion rate.[100] Conversely, the popular fractional anisotropy (FA) parameter entangles information about microscopic anisotropy and orientation dispersion[101] and may be expressed as a function of more fundamental metrics reporting exclusively on the underlying anisotropy and orientation properties.[71] Analogously, conventional kurtosis metrics[70] contain aggregated information about intra-compartmental deviations from non-Gaussian diffusion and various kinds of inter-compartmental (or intravoxel) heterogeneity.[102] Neglecting intra-compartmental kurtosis, the metrics $\text{V}[D_{\text{iso}}]$ and $\text{E}[D_\Delta^2]$, including their literature counterparts, may be related to the isotropic, anisotropic, and total kurtosis.[56,71,102] Consequently, the $\Delta_{\omega/2\pi}\text{V}[D_{\text{iso}}]$ and $\Delta_{\omega/2\pi}\text{E}[D_\Delta^2]$ metrics report on the isotropic and anisotropic contributions to time- and frequency-dependence of the mean kurtosis.[103]

III. METHODS

A. Simulations

The random permeable barrier model (RPBM) in Eq. (9) was used to simulate signals for two acquisition schemes exploring (a) narrow and (b) wide frequency ranges at constant number of data points. The protocols were based on double-rotation waveforms with (a) 36 b-values, $n = 0$, and $\tau = 5$ ms, as well as (b) 4 b-values; $n = 0, 1, 3, 7, 15, 31, 63, 127,$ and 255; and $\tau = 256$ ms. Both the protocols used waveforms with $\varepsilon_{\text{up}} = 0.001\tau$, $\varepsilon_{\text{down}} = 0.002\tau$, and $\Delta\psi_2 = 2\pi$; b values geometrically spaced between 0.5 and 4×10^9 s m^{-2}; $b_\Delta = 1, 0,$ and -0.5; $b_\eta = 0$; eleven rotations ($\Psi = 0, \Theta, \Phi$) taken from the electrostatic repulsion scheme,[104] and a single acquisition with $b = 0$, yielding a total of 1189 acquisitions with different waveforms. Each waveform $\mathbf{g}(t)$ was discretized in 1000 time steps, and
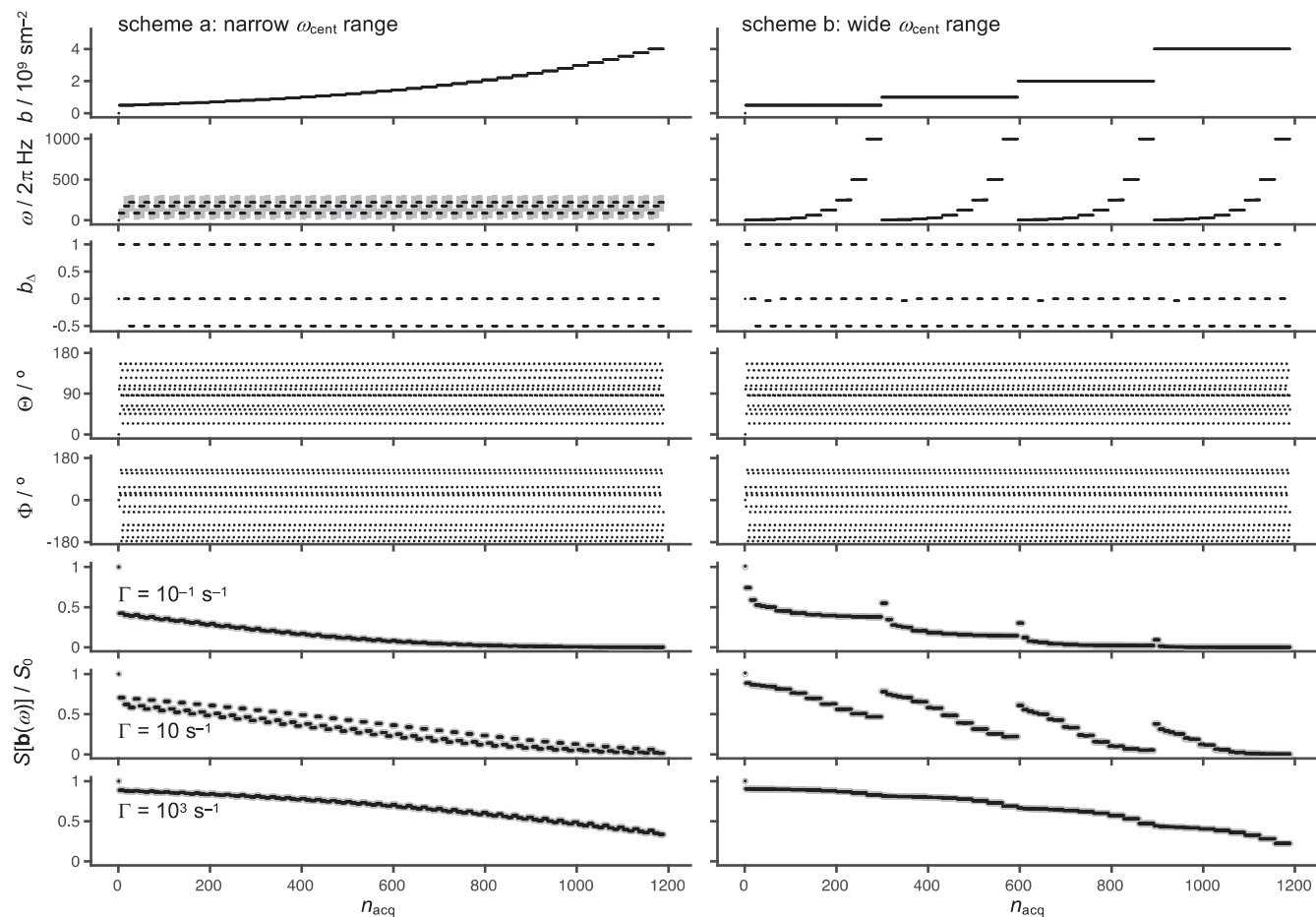
FIG. 3. Examples of acquisition schemes and corresponding signals calculated for the random permeable barrier model (RPBM). The acquisition schemes are shown as plots of magnitude b, frequency ω, normalized anisotropy b_Δ, and orientation (Θ, Φ) of the tensor-valued encoding spectrum $\mathbf{b}(\omega)$ vs the acquisition number n_{acq}. Diffusion encoding was performed with double-rotation gradient waveforms of the type shown in Fig. 2(b), giving encoding power over a range of frequencies represented by the vertical gray lines from the tenth to the 90th percentiles and black dots indicating the centroid frequency ω_{cent}. The left and right columns feature schemes with narrow and wide ranges of ω_{cent}, respectively. The simulated signals $S[\mathbf{b}(\omega)]$ (gray circles) were obtained with the RPBM using high-ω diffusivity $D_0 = 2 \times 10^{-9}$ m^{2}s^{-1}, low-ω diffusivity $D_\infty = 0.2 \times 10^{-9}$ m^{2}s^{-1}, and characteristic transition rate Γ, as indicated in the three bottom panels to the left. The fitted signals (black dots) were back-calculated from the $\mathbf{D}(\omega)$ distributions obtained by Monte Carlo inversion of the simulated signals. The signals were normalized with the fitted signal S_0 extrapolated to $b = 0$ according to Eq. (40).

the tensor-valued encoding spectra $\mathbf{b}(\omega)$ were obtained by numeric evaluation of Eqs. (13), (15), and (16) using zero-filling in the time domain and resampling in the frequency domain to 500 linearly spaced frequencies from 0 to 1200 Hz. The acquisition protocols are shown in the top panels of Fig. 3 using values of b, ω_{cent}, and b_Δ numerically recalculated from the discretized $\mathbf{b}(\omega)$ using Eqs. (17)–(20). Correspondingly, (Θ, Φ) was extracted from the eigenvectors corresponding to the b_{ZZ} eigenvalue obtained by diagonalization of $\mathbf{b}$. The ω vs acquisition number n_{acq} panels in Fig. 3 show both ω_{cent} and the tenth to 90th percentile ω-ranges of each $b(\omega)$, illustrating that scheme a exhibits a similar ω range within each acquisition as the spread of ω_{cent} between acquisitions. For both

the schemes, the encoding power is centered on $\omega/2\pi$ of ~200 Hz, as shown in Fig. 4. Using $\mathbf{D}(\omega)$ from the RPBM in Eq. (9) and $\mathbf{b}(\omega)$ obtained from $\mathbf{g}(t)$ as described above, signals $S[\mathbf{b}(\omega)]$ were calculated by numeric evaluation of Eq. (30) under the condition $\langle \mathbf{v} \rangle = 0$.

B. Experiments

MRI phantoms with well-defined diffusion properties were assembled from NMR tubes with yeast cell sediment, salt solution, lamellar liquid crystal, and water. Magnesium nitrate hexahydrate, cobalt nitrate hexahydrate, and 1-decanol were purchased from
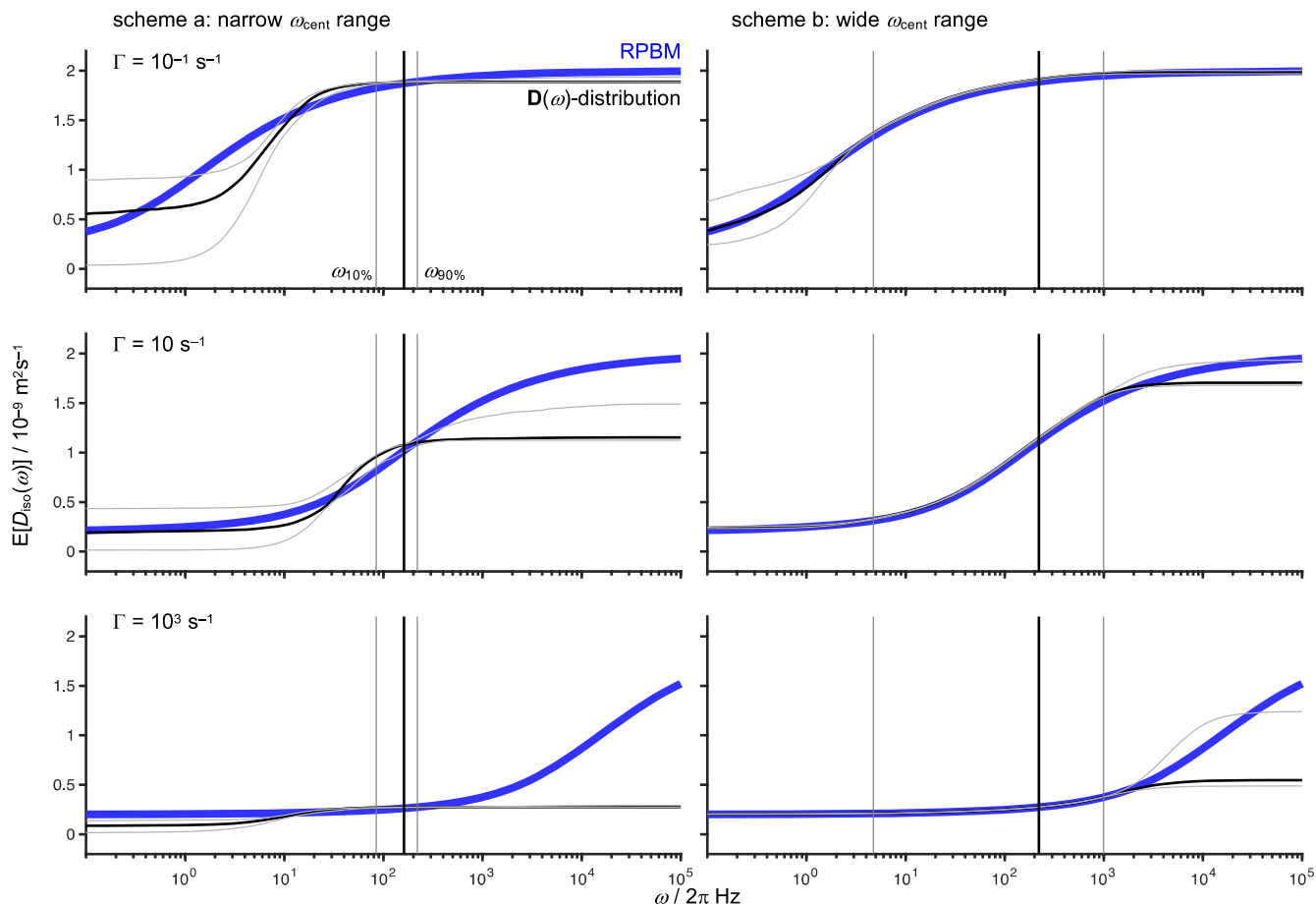
FIG. 4. Mean isotropic diffusivity $E[D_{iso}(\omega)]$, defined in Eqs. (11) and (37), calculated with the RPBM (blue lines) and from the $D(\omega)$ distributions obtained by Monte Carlo inversion of the simulated signal data shown in Fig. 3 (tenth, 50th, and 90th percentiles over bootstrap replicates shown with the gray, black, and gray lines, respectively) using acquisition protocols with narrow (left) and wide (right) ω_{cent} ranges illustrated with the vertical lines (tenth, 50th, and 90th percentiles of the b-weighted ω_{cent} distributions represented by the gray, black, and gray lines, respectively).

Sigma-Aldrich Sweden AB, sodium octanoate from J & K Scientific via Th. Geyer in Sweden, and fresh baker's yeast (trade name: Kronjäst) from a local supermarket. Unless otherwise stated, water was purified with a Millipore-Q system. The yeast sample was prepared by dispersing a block of yeast in an equal amount of tap water, transferring 1 ml of the cell suspension to a 5 mm NMR tube, and allowing the cells to sediment under the action of gravity at 4 °C overnight.[105] To remove water-soluble nutrients and metabolites contributing to water T_2-relaxation via proton chemical exchange, the cells in the tube were washed by three cycles of removing the supernatant with a syringe, adding 2 ml tap water, resuspending by vigorous shaking, and renewed sedimentation at 4 °C. The aqueous salt solution comprised saturated magnesium nitrate[106] doped with cobalt(II) nitrate to reach T_2 of about 100 ms. The lamellar liquid crystal was prepared from 85.79 wt. % water, 9.17 wt. %

1-decanol, and 5.04 wt. % sodium octanoate.[107] A composite phantom was assembled by inserting 4 mm NMR tubes with salt solution and liquid crystal into a 10 mm NMR tube with water.

Experiments on *ex vivo* rat brain were approved by the Animal Committee of the Provincial Government of Southern Finland in accordance with the European Union Directives 2010/63/EU. A healthy adult rat Sprague–Dawley was transcardially perfused with 0.9% saline, followed by 4% paraformaldehyde in 0.1M phosphate buffer (pH = 7.4). After extraction, the brain was sagittally sectioned along the brain midline and placed in a solution of phosphate buffered saline 0.1M and gadoteric acid 50 μl/10 ml (Dotarem 279.3 mg/ml; Guerbet, France) for 24 h. During MRI measurements, the brain was immersed in perfluoropolyether (Galden; TMC Industries, USA) within a 10 mm NMR tube.

TABLE I. MRI acquisition and processing parameters.

	Phantoms	*Ex vivo* rat brain	Excised tumor
Spectrometer	Avance-Neo	Avance-III HD	Avance-III HD
Magnetic field / T	11.7	11.7	14.0
Acquisition software	TopSpin 4.0.7	ParaVision 6.0.1	TopSpin 3.5.6
Image read-out	RARE	MSME	RARE
Acquisition resolution / mm^3	$0.15 \times 0.3 \times 1$	$0.09 \times 0.09 \times 0.09$	$0.15 \times 0.3 \times 1$
Matrix size	$32 \times 16 \times 1$	$111 \times 111 \times 10$	$32 \times 16 \times 1$
Diffusion gradient duration / ms	25	8	10
Max b-value / 10^9 sm^{-2}	6.4	3.5	11
Double-rotation ratio n	0, 1, 2, 3, 4, 5	0	0
Range centroid frequency ω_{cent} / 2π Hz	20–260	53–160	44–140
Normalized anisotropy b_Δ	-0.5, 0, 0.5, 1	-0.5, 0, 0.5, 1	-0.5, 0, 0.5, 1
No. directions	15	11	15
No. acquired volumes	2880	312	480
Echo time / ms	74.5	21.2	52.5
Repetition time / s	5.1	0.2	1.1
Measurement time / h	4	50	0.3
Reconstruction software	Matlab R2018b	ParaVision 6.0.1	Matlab R2018b
Reconstructed voxel size / mm^3	$0.15 \times 0.15 \times 1$	$0.09 \times 0.09 \times 0.09$	$0.15 \times 0.15 \times 1$

Human neuroblastoma cells were cultured at 37 °C and 5% CO_2 in complete medium (RPMI 1640 supplemented with 10% fetal bovine serum and 1% penicillin/streptomycin). A female BALB/c mouse (Janvier Labs, France) was s.c. inoculated with 2×10^6 tumor cells.[76] After ~5 weeks, the mouse was sacrificed; the tumor was removed and immediately transferred to a 10 mm NMR tube containing 4% formaldehyde in phosphate buffer solution (Histolab, Sweden). The sample was stored at room temperature for 1 day before being investigated with MRI.

MRI measurements were performed on three different Bruker spectrometers (Karlsruhe, Germany) equipped with MIC-5 probes, giving up to 3 Tm^{-1} gradient amplitude on-axis. Diffusion encoding employed pairs of double-rotation gradient waveforms bracketing the 180° pulse in a spin echo sequence.[71] Numerical calculation of $\mathbf{b}(\omega)$ included all the diffusion and imaging gradients between the centers of the excitation pulse and the spin echo. Additional acquisition and processing parameters are presented in Table I and detailed acquisition protocols are shown in Figs. 5 and 6. Reconstructed images were exported to NIfTI format for further analysis with the *md-dmri* Matlab toolbox.[108]

C. Monte Carlo data inversion and extraction of relevant metrics

Monte Carlo inversion of simulated and experimental signals $S[\mathbf{b}(\omega)]$ into nonparametric $\mathbf{D}(\omega)$ distributions in the $[D_\parallel, D_\perp, \theta, \phi, D_0, \Gamma_\parallel, \Gamma_\perp]$ space was performed with the MATLAB code available at https://github.com/daniel-topgaard/md-dmri using $D_\parallel$, $D_\perp$, and D_0 limited to the range from 5×10^{-12} to 5×10^{-9} m^{2}s^{-1}, $\Gamma_\parallel$ and $\Gamma_\perp$ in the range from 0.1 to 10^5 s^{-1}, 20 steps of proliferation, 20 steps of mutation/extinction, 200 input components per step

of proliferation and mutation/extinction, ten output components, and bootstrapping by 100 repetitions using random sampling with replacement. For each of the 100 bootstrap replicates and ten components i, the values of $D_{\parallel,i}$, $D_{\perp,i}$, $D_{0,i}$, $\Gamma_{\parallel,i}$, and $\Gamma_{\perp,i}$ were converted to $D_{\parallel,i}(\omega)$ and $D_{\perp,i}(\omega)$ at specific values of ω, using Eqs. (33) and (34) and, subsequently, to $D_{iso,i}(\omega)$, $D_{\Delta,i}{}^2(\omega)$, and $\mathbf{D}_i(\omega)$ with Eqs. (11), (32), and (35). For each of the 100 bootstrap replicates, total and bin-resolved signals S_0; fractions f_{binn}; statistical descriptors E[X], V[X], and C[X,Y]; and frequency-dependence metrics $\Delta_{\omega/2\pi}$E[X], $\Delta_{\omega/2\pi}$V[X], and $\Delta_{\omega/2\pi}$C[X,Y] were calculated with Eqs. (36)–(41) using the limits bin1: $D_{iso} < 1 \times 10^{-9}$ m^{2}s^{-1} and $D_\Delta^2 > 0.25$; bin2: $D_{iso} < 1 \times 10^{-9}$ m^{2}s^{-1} and $D_\Delta^2 < 0.25$; and bin3: $D_{iso} > 1 \times 10^{-9}$ m^{2}s^{-1}. Finally, display parameters med(S_0) and med(E[X]) were obtained by taking the medians over the 100 bootstrap replicates. To simplify the notation, the median operators are not shown explicitly in the following text and figures.

IV. RESULTS

Figure 3 shows signals $S[\mathbf{b}(\omega)]$ calculated with Eq. (30) for a tensor-valued diffusion spectrum $\mathbf{D}(\omega)$ with all the eigenvalues given by the random permeable barrier model (RPBM) in Eq. (9) using three values of the characteristic transition rate Γ. The two acquisition schemes rely on double-rotation gradient waveforms (see Fig. 2) to cover the narrow and wide ranges, respectively, of centroid frequencies ω_{cent} defined from the tensor-valued encoding spectrum $\mathbf{b}(\omega)$ via Eqs. (18) and (20). Visual inspection of the data in Fig. 3 reveals the absence of signal modulations from the acquisition parameters b_Δ, Θ, and Φ at constant b and ω_{cent}, indicating isotropic diffusion. Conversely, modulations as a function of ω_{cent} at constant b, b_Δ, Θ, and Φ show that diffusion is ω-dependent (restricted)
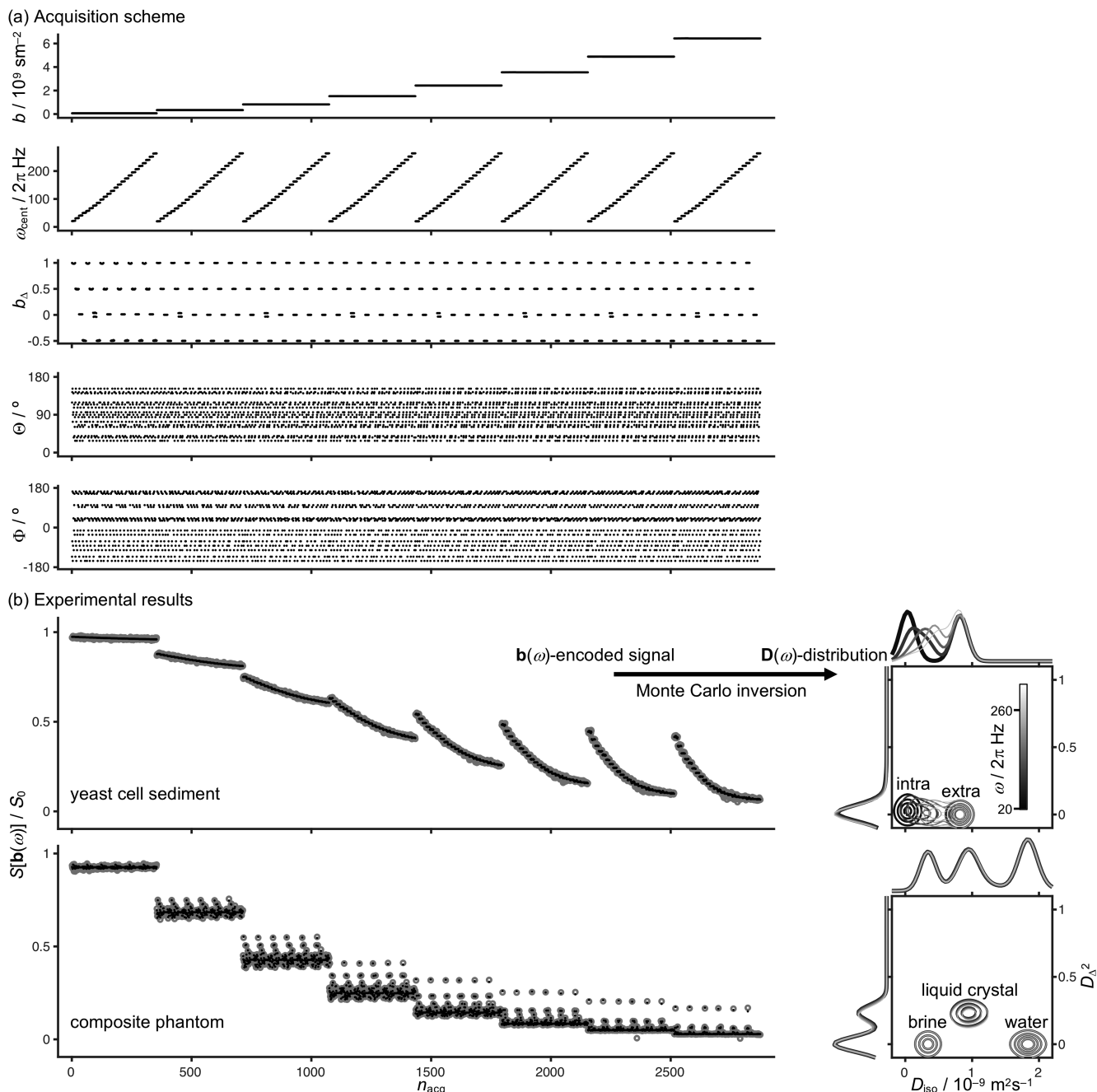
FIG. 5. Comprehensive acquisition scheme and experimental results for $\mathbf{b}(\omega)$-encoded diffusion MRI. (a) Magnitude b, centroid frequency ω_{cent}, normalized anisotropy b_Δ, and orientation (Θ, Φ) of the tensor-valued encoding spectrum $\mathbf{b}(\omega)$ vs the acquisition number n_{acq} with the maximum value 2880. Diffusion encoding was performed with pairs of gradient waveforms of the type shown in Fig. 2(b) with 25 ms duration and 3 Tm^{-1} maximum amplitude. (b) Experimental data (circles: measured, points: back-calculated from the $\mathbf{D}(\omega)$ distributions) obtained at 11.7 T on a yeast cell sediment and a composite phantom comprising an assembly of glass tubes with pure water, a saturated salt solution (brine), and a lamellar liquid crystal. Monte Carlo inversions of the $\mathbf{b}(\omega)$-encoded signals yield $\mathbf{D}(\omega)$ distributions shown in the panels to the right as projections onto the 2D plane and 1D axes of the isotropic diffusivity D_{iso} and squared normalized anisotropy D_Δ^2 for five values of ω (indicated with the linear gray scale of contour lines). The intracellular water in the yeast is restricted (ω-dependent), while the four other water pools are Gaussian (ω-independent) within the investigated range from 20 to 260 Hz.
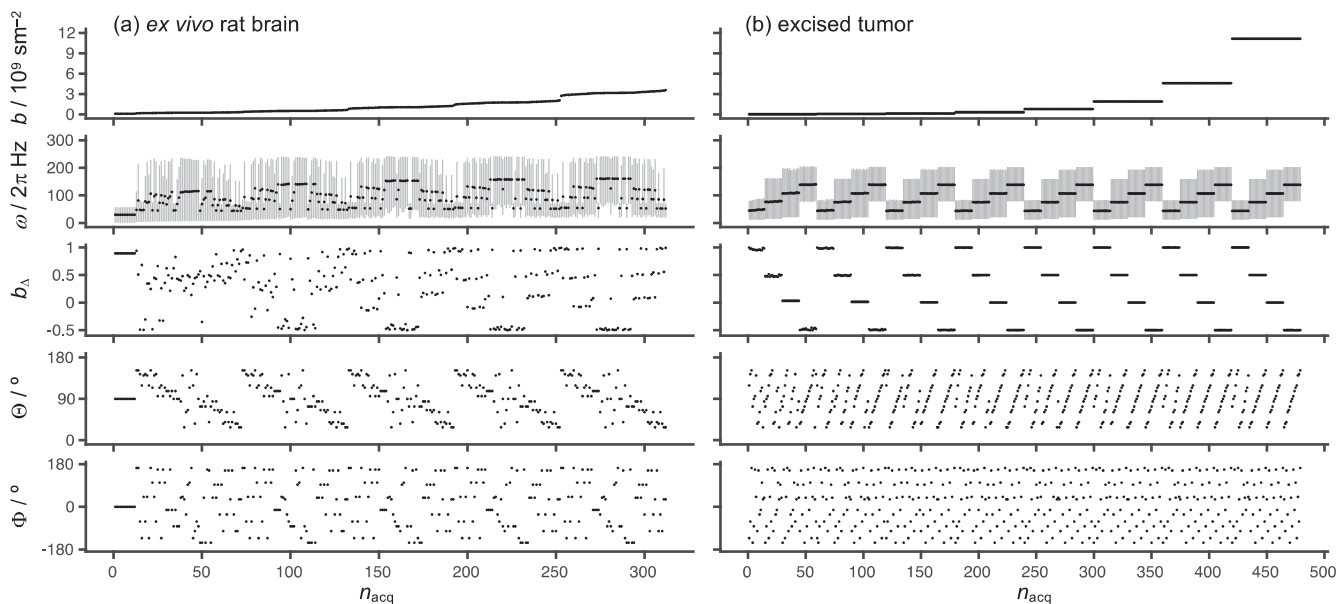
FIG. 6. Abbreviated acquisition schemes based on the 2880-point comprehensive one shown in Fig. 5. (a) *Ex vivo* rat brain scheme with 312 points limited to $\omega_{cent}/2\pi$ from 53 to 160 Hz and b values up to 3.6×10^9 sm^{-2}. (b) Excised tumor scheme with 480 points limited to $\omega_{cent}/2\pi$ from 44 to 140 Hz and b values up to 11×10^9 sm^{-2}. In the ω panels, the black dots indicate ω_{cent}, while the vertical gray lines show the tenth to 90th percentiles of $b(\omega)$.

within the investigated ω_{cent} range. The effects of restriction are most clear for the wide ω_{cent}-range scheme and the intermediate value of Γ.

Monte Carlo inversion of Eq. (30) using the axisymmetric Lorentzian approximation in Eqs. (32)–(34) yields $\mathbf{D}(\omega)$ distributions, which, upon back-calculation of $S[\mathbf{b}(\omega)]$ with Eq. (30), perfectly reproduces the results from the RPBM. The ω dependencies of the mean isotropic diffusivity $E[D_{iso}(\omega)]$ of the obtained $\mathbf{D}(\omega)$ distributions and the ground-truth RPBM are compared in Fig. 4, showing general agreement within the ω_{cent} range defined by the acquisition scheme. Outside this range, the $\mathbf{D}(\omega)$ distributions are highly variable across the bootstrap replicates, illustrating the challenges of estimating both the low- and high-ω plateaus. For the narrow ω_{cent}-range scheme, minor systematic differences between the $\mathbf{D}(\omega)$ distributions and the RPBM can be discerned, particularly for the intermediate Γ case despite the fact that the signals are perfectly overlapping, as shown in Fig. 3. At the finite noise levels and more limited exploration of the acquisition variable space in most experimental studies, the smooth low-ω to high-ω transition of the RPBM would consequently be indistinguishable from a smooth transition originating from a distribution of Lorentzians. Contrarily, we do not expect the inherently smooth RPBM to have a general ability to reproduce the sharper transitions for a single Lorentzian or the planar, cylindrical, or spherical compartments.

Experimental demonstration of our approach is shown in Fig. 5 for two samples with well-defined and previously investigated restriction and anisotropy properties,[37] namely, a yeast cell sediment[105] and an assembly of glass tubes with pure water,[109] saturated salt solution,[106] and lamellar liquid crystal.[107] In the case of isotropic Gaussian diffusion, the signal attenuation is completely

determined by the value of b and independent of all other variables ω_{cent}, b_Δ, Θ, and Φ. The observed sensitivity to $\omega_{cent}/2\pi$ in the investigated range 20–260 Hz for the yeast cell sediment indicates restriction in micrometer-scale compartments, while the dependence on b_Δ for the composite phantom reveals anisotropy. These qualitative observations of restriction and anisotropy from the raw signal data are filled in with more details by the obtained $\mathbf{D}(\omega)$ distributions: The yeast sample comprises two isotropic ($D_\Delta{}^2 = 0$) pools, one Gaussian (ω-independent) and one restricted (ω-dependent) originating from the extra- and intra-cellular spaces, respectively, separated by the virtually impermeable plasma membranes.[110] The composite phantom yields three Gaussian pools, one of which being anisotropic with a value $D_\Delta{}^2 = 0.25$ consistent with the essentially two-dimensional diffusion of water confined to the nanometer-scale gaps between the planar detergent bilayers in a lamellar liquid crystal.[68] With frequencies on the scale of 10^9 Hz, it would be possible to observe the effects of restricted diffusion across these gaps. Correspondingly, frequencies approaching 10^{12} Hz would allow investigating the regime of ballistic motion of the individual water molecules.[111] These high-ω regimes are, however, far beyond the range accessible with MRI methods based on magnetic field gradients.

Figure 7 shows the data for a few representative voxels in an *ex vivo* rat brain. The $\mathbf{D}(\omega)$ distributions for voxels in pure white matter (WM), gray matter (GM), and phosphate buffered saline (PBS) in the ventricles are qualitatively consistent with the earlier *in vivo* mouse results[59] (WM: low D_{iso} and high $D_\Delta{}^2$, GM: low D_{iso} and low $D_\Delta{}^2$, and PBS: high D_{iso} and low $D_\Delta{}^2$) with only barely detectable ω-dependence in the investigated range from 53 to 160 Hz. The voxel in the granule cell layer in the dentate gyrus
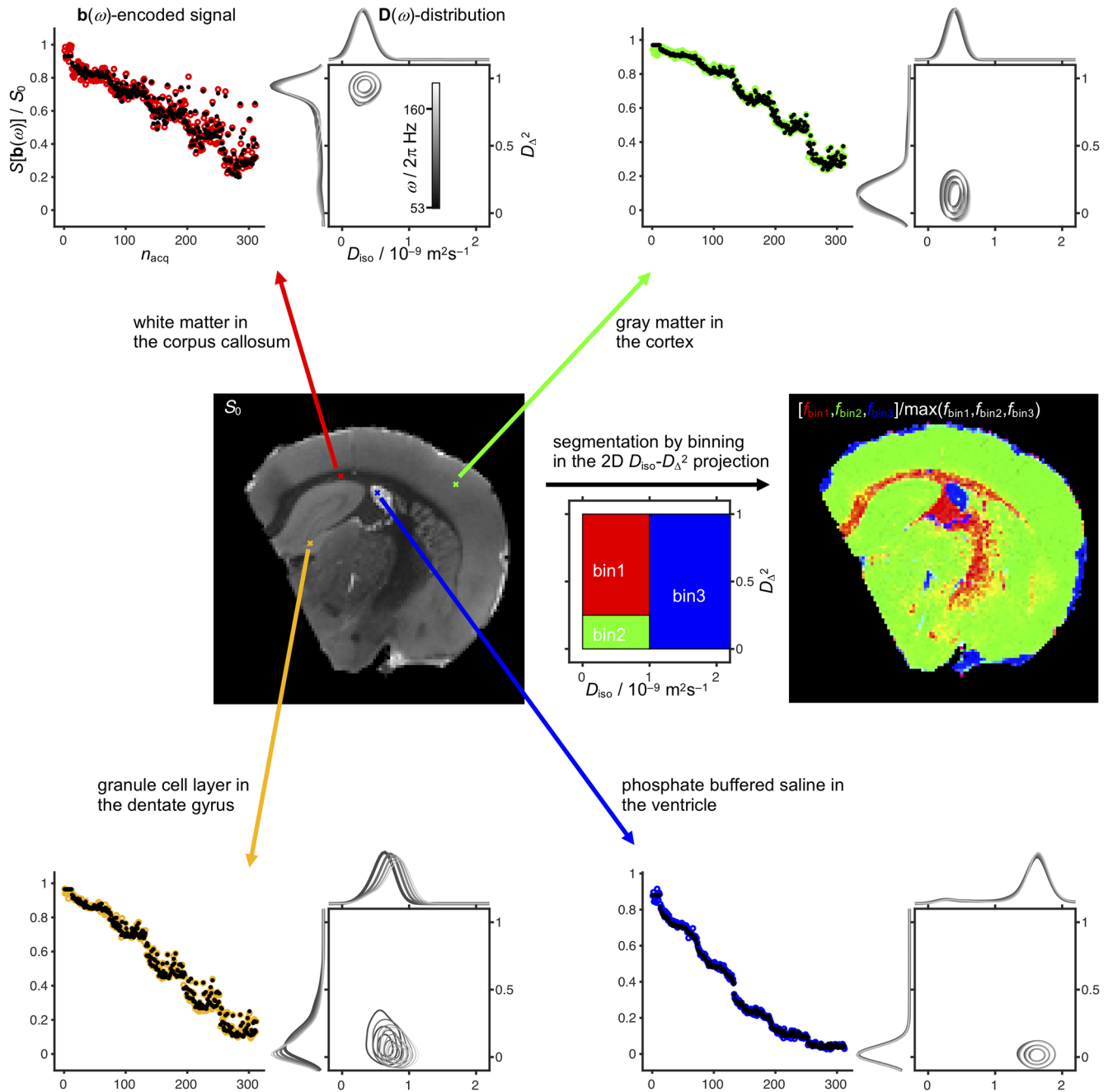
FIG. 7. $\mathbf{D}(\omega)$ distributions for selected voxels in the *ex vivo* rat brain. The figures show $\mathbf{b}(\omega)$-encoded signals, according to the scheme shown in Fig. 6(a), and corresponding $\mathbf{D}(\omega)$ distributions for the four voxels indicated with crosses in the S_0 map, see Eq. (40). The results for the individual voxels at $\omega/2\pi = 53$ Hz guide the division of the 2D D_{iso}-D_Δ^2 projection into three bins—nominally specific for white matter, gray matter, and phosphate buffered saline—for the purpose of image segmentation by coding the per-bin signal fractions f_{bin1}, f_{bin2}, and f_{bin3} into RGB colors and extraction of bin-specific diffusion metrics according to Eqs. (36)–(41). The voxels from the granule cell layer in the dentate gyrus and white matter show the hallmarks of restriction (ω-dependence) and anisotropy ($D_\Delta^2 \approx 1$), respectively.

gives a $\mathbf{D}(\omega)$ distribution resembling the one from GM, but with a more pronounced ω-dependence in agreement with earlier observations using oscillating gradient encoding.[95] The ω-dependence is consistent with granule cell dimensions on the 10 μm scale as seen in histology.[112] The $\mathbf{D}(\omega)$ distributions for WM, GM, and PBS guide the definition of the three bins in the 2D D_{iso}-D_Δ^2 projection to generate maps of nominally tissue type-specific per-bin signal fractions and diffusion metrics. Figure 8 shows the maps of per-voxel and bin-
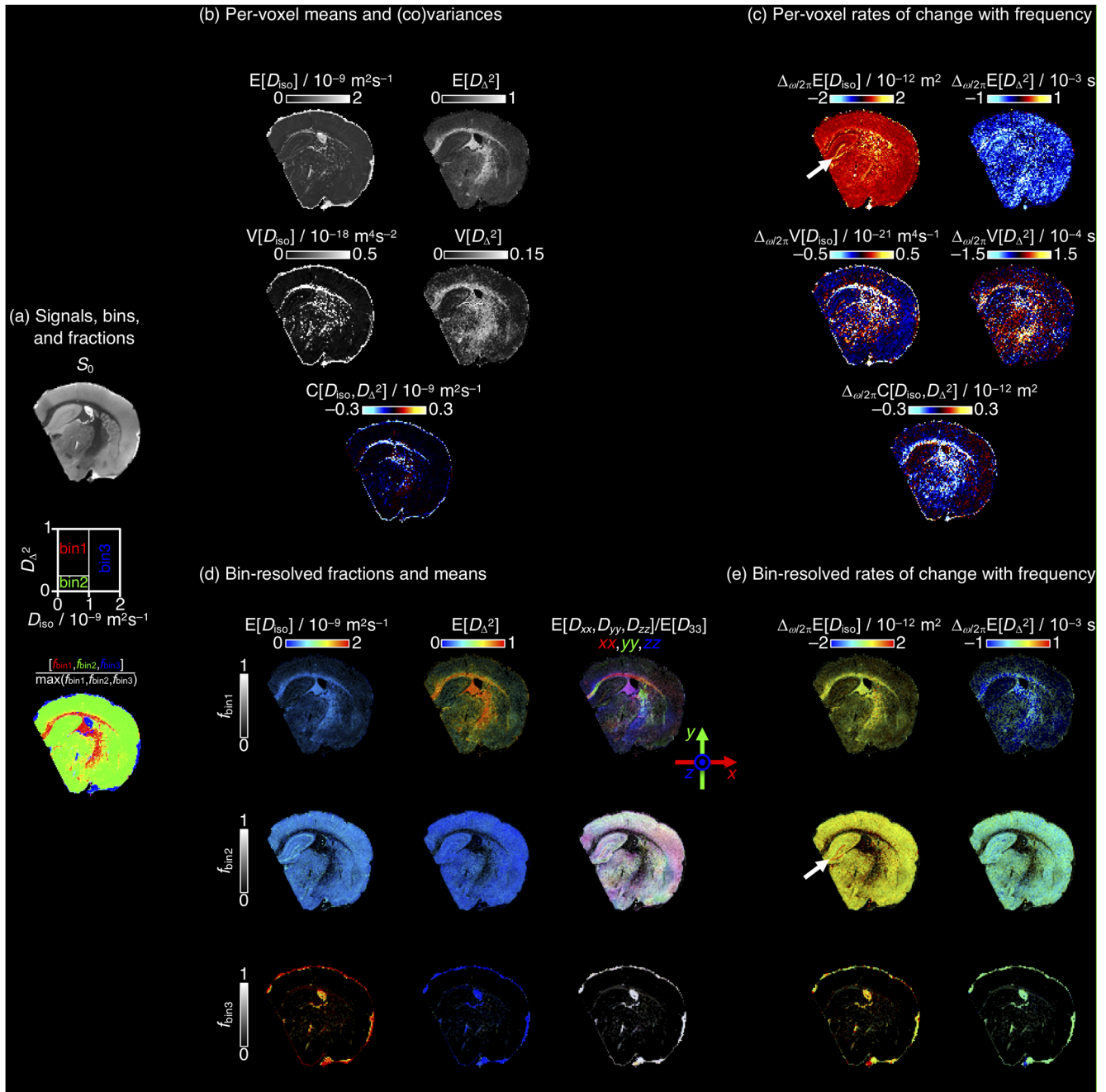
FIG. 8. Parameter maps calculated from the per-voxel $\mathbf{D}(\omega)$ distributions for the *ex vivo* rat brain using Eqs. (36)–(41). (a) S_0 map, definition of bins in the 2D D_{iso}-D_Δ^2 projection, and map of per-bin signal fractions [f_{bin1}, f_{bin2}, f_{bin3}] coded into RGB colors. (b) Per-voxel statistical descriptors E[X], V[X], and C[X, Y] over the D_{iso} and D_Δ^2 dimensions of the $\mathbf{D}(\omega)$ distributions evaluated at a selected frequency $\omega/2\pi = 53$ Hz. (c) Rates of change with frequency, $\Delta_{\omega/2\pi}$E[X], $\Delta_{\omega/2\pi}$V[X], and $\Delta_{\omega/2\pi}$C[X, Y], of the per-voxel metrics highlighting areas with effects of restricted diffusion. (d) Bin-resolved signal fractions and means E[X] of the diffusion metrics at 53 Hz coded into image brightness (vertical brightness bars) and blue–green–red color scale (horizontal color bars). Color-coding of orientation derives from the lab-frame (shown with the red, green, and blue arrows) diagonal values [D_{xx}, D_{yy}, D_{zz}] normalized by the maximum eigenvalue D_{33}. (e) Bin-resolved rates of change with frequency over the range 53–160 Hz. The white arrows in panels (c) and (e) indicate elevated values of $\Delta_{\omega/2\pi}$E[D_{iso}] for the granule cell layer in the dentate gyrus.

resolved statistical descriptors $E[D_{iso}]$, $E[D_\Delta^2]$, $V[D_{iso}]$, $V[D_\Delta^2]$, and $C[D_{iso},D_\Delta^2]$, typically associated with tensor-valued encoding,[12,58] and rates of change of the diffusion metrics with frequency, for instance, $\Delta_{\omega/2\pi}E[D_{iso}]$ often used to display the results from oscillating gradient encoding,[24,95,96] as well as novel metrics correlating information about restriction and anisotropy. Of special note in this latter category is the separation of high- and low-D_Δ^2 components with similar D_{iso} (bin1 and bin2), and the association of the
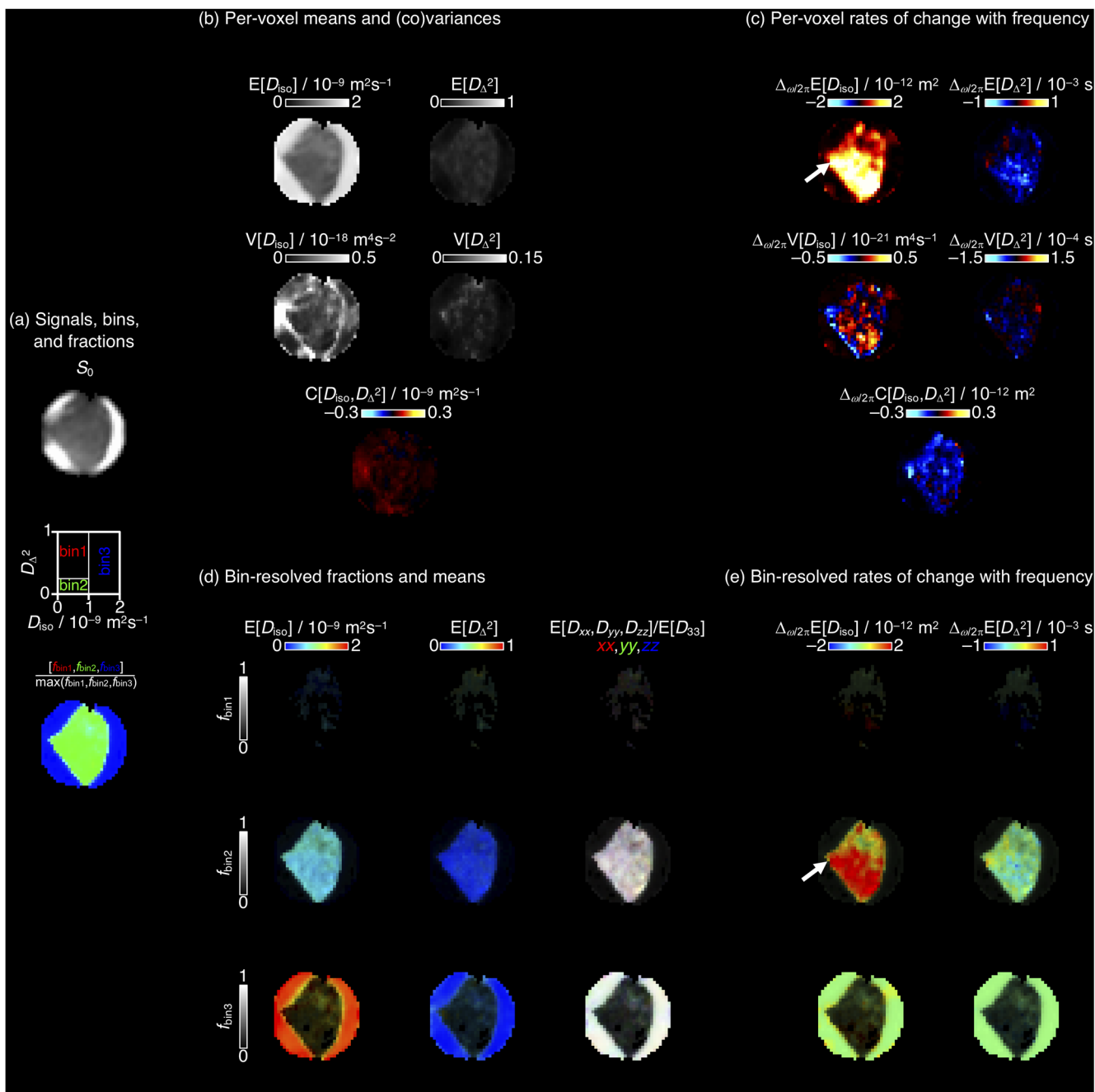

FIG. 9. Parameter maps for part of an excised tumor immersed in an aqueous formaldehyde solution using the acquisition scheme shown in Fig. 6(b). See the caption of Fig. 8 for detailed explanation of the panels. The arrows in panels (c) and (e) show tumor areas with pronounced effects of restricted diffusion.

03 September 2024 10:04:04

effects of restricted diffusion to the low-D_Δ^2 component (bin2), as shown in Fig. 8(e).

The maps of the excised tumor shown in Fig. 9 feature an extended area with pronounced effects of restricted diffusion (high $\Delta_{\omega/2\pi}E[D_{iso}]$) as well as regions with high $V[D_{iso}]$ resulting from the co-existence of low- and high-D_{iso} water pools within the same imaging voxel, tentatively originating from dense tumor and formaldehyde solution or tissues with degraded cell membranes. These maps may permit non-invasive resolution of apoptotic, necrotic, and viable tumor tissues having distinctly different cell densities, sizes, shapes, and membrane properties.

V. DISCUSSION

The set of experimental data demonstrates that our proposed model-free approach enables the estimation of quantitative metrics related to restricted and anisotropic diffusion within a single set of measurements, thereby merging oscillating gradient and tensor-valued encoding into a common experimental and analysis framework. Although the complete tensor-valued encoding spectra $\mathbf{b}(\omega)$ are used in the data inversion, the acquisition schemes shown in Figs. 5 and 6 are reported in terms of the five variables b, Θ, Φ, ω_{cent}, and b_Δ, see definitions in Eqs. (17)–(20). These variables provide a convenient short-hand notation of the investigated diffusion properties and are all familiar from the literature—the first three being the b value and b vector of diffusion tensor imaging,[36,85] the fourth being the characteristic encoding frequency of oscillating gradients,[19,24,65] and the fifth being the normalized anisotropy of tensor-valued encoding.[38] At high ω_{cent} and $b_\Delta = 0$, the signal as a function of b depends solely on the distribution of high-ω isotropic diffusivities. Decreasing ω_{cent} and using non-zero values of b_Δ bring in the effects of restriction and anisotropy, respectively. At the lowest values of ω_{cent} and $b_\Delta = 1$, these effects are maximized and the variation of signal with (Θ, Φ) gives information about the orientations of anisotropic compartments. Conventional diffusion MRI[36,85] is performed in this latter limit and is sensitive to all the microstructural properties without being able to resolve their individual contributions.[63] Sampling of the multidimensional space spanned by all five effective acquisition variables, on the other hand, allows retrieval of the corresponding multidimensional $\mathbf{D}(\omega)$ distributions with information about diffusivity, orientation, restriction, anisotropy, and their correlations.

The quality of the fits in Figs. 3 and 5 show that our proposed signal expression, being the sum of contributions from components with $\mathbf{D}(\omega)$ approximated as tensor-valued Lorentzians, see Eqs. (32)–(34), is sufficiently flexible to capture all relevant signal modulations over exhaustive ranges of acquisition variables for both the random permeable barrier model and the investigated samples selected for their well-known effects of restrictions and anisotropy. Correspondingly, the obtained $\mathbf{D}(\omega)$ distributions shown in Figs. 5 and 7 and derived parameter maps shown in Figs. 8 and 9 are all consistent with the design of the phantoms and previous results in the literature,[37,95,105,106,109] showing that the good fits do not come at the expense of excessive overfitting that would lead to spurious peaks in the distributions and noisy parameter maps. Despite the successful data fitting and reproduction of expected results, we emphasize that the proposed approximation is merely a convenient

mathematical representation that yields an acceptable compromise between physical correctness, mathematical convenience, and utility for solving scientific questions without tempting the user to overinterpretation.

With the comprehensive 2880-point acquisition scheme shown in Fig. 5, the presence of restriction and anisotropy can be deduced by simple visual inspection of the signal intensities as a function of the acquisition variables—especially ω_{cent} and b_Δ for a given value of b—and quantified from the 2D D_{iso}-D_Δ^2 projections of the obtained $\mathbf{D}(\omega)$ distributions. Admittedly, the data shown in Fig. 5 were acquired under exceptionally favorable circumstances, using 3 Tm^{-1} gradient hardware and samples with sufficiently large values of the transverse relaxation time T_2 to allow for in total 0.050 s of diffusion-encoding gradients and the broad frequency range 20–260 Hz even at the highest b value 6.4 × 10^9 sm^{-2}. Conversely, the data shown in Figs. 7–9 represent more realistic conditions with short-T_2 fixated tissues and abbreviated acquisition schemes comprising only 312 or 480 data points over the limited ranges 53–160 or 44–140 Hz. Despite these limitations, the data shown in Fig. 8 reproduce earlier findings on both restriction[95] and anisotropy[59] in the rodent brain, as well as bring novel information on the correlations between the properties. The number of acquisitions is comparable to the 10 min and 300 point schemes used in early clinical implementations of tensor-valued encoding for studies of brain tumors,[72] later to be truncated and optimized for 3 min measurements consistent with applications in clinical practice,[79] thus indicating the potential for the implementation of our proposed method for both clinical and pre-clinical research studies—initially maybe by simply interleaving the latest protocols for oscillating gradient[24] and tensor-valued encoding[81] using identical pulse sequences and imaging settings.

Our analysis relies on the Gaussian phase distribution approximation,[18,84] the validity limits of which have been investigated in the diffusion NMR literature.[113,114] In the extreme case of porous media with well-defined compartment sizes and/or inter-compartment distances as well as optimal acquisition parameters where both the wavelength of the dephasing vector $\mathbf{q}(t)$, see Eq. (13), and the diffusional displacement matches some structural length scale, the phase distribution may include sharp edges or multiple maxima, leading to signal attenuation with diffraction-like features, as observed for polystyrene sphere packs,[115] water-in-oil emulsions,[116] cylinders,[117] and red blood cells.[118] At diffusional displacements smaller than the characteristic length scales, deviations from the Gaussian phase distribution approximation give rise to signal decay that appears multiexponential and may be misinterpreted as originating from multiple separate compartments.[119] For biological tissues with less ideal pore geometries studied with less optimal acquisition parameters, the deviations may be challenging to distinguish from the often overwhelming effects of various sources of intravoxel heterogeneity that are quantified with, for instance, the variance and covariance metrics in Eqs. (38) and (39). In contemporary diffusion MRI literature, the more subtle deviations from the Gaussian phase distribution approximation are often termed intra-compartmental kurtosis, which may be teased apart from other sources of kurtosis using the correlation tensor approach relying on a rather specific double diffusion encoding acquisition protocol and a truncated cumulant expansion analysis.[102] As our current acquisition protocol, combining oscillating gradients and

tensor-valued encoding, do not fulfill the conditions for correlation tensor analysis, we are here unable to estimate the effects of intra-compartmental kurtosis. If deviations from the Gaussian phase distribution are indeed present, we expect that our analysis based on Eq. (30) yields bias in the estimated values of, in particular, $E[D_\Delta^2]$, $V[D_{iso}]$, $\Delta_{\omega/2\pi}E[D_{iso}]$, $\Delta_{\omega/2\pi}V[D_{iso}]$, and $\Delta_{\omega/2\pi}E[D_\Delta^2]$. Modifying the correlation tensor analysis to be applicable to our type of experimental data is, however, beyond the scope of this paper.

VI. CONCLUSION

In this work, we have taken a crucial step toward model-free investigations of restriction and anisotropy in heterogeneous biological tissues, having potentially far-reaching implications for our understanding of microstructural changes associated with pathology or normal brain development. Through simulations and measurements on phantoms, *ex vivo* rat brain, and excised tissue from a mouse model of human neuroblastoma, we demonstrated that our proposed model-free approach is sufficiently flexible to capture the signal modulations for extreme cases of restriction and anisotropy over exhaustive ranges of acquisition variables, while still being robust enough to give quantitative parameter maps reporting on relevant microstructural properties using abbreviated measurement protocols compatible with clinical research studies.

ACKNOWLEDGMENTS

AUTHOR DECLARATIONS

Conflict of Interest

The authors have no conflicts to disclose.

Author Contributions

O.N. and A.S.: preparation of rat brain; acquisition, processing, and interpretation of MRI data. M.Y.: development of ParaVision data acquisition code and Matlab conversion code; acquisition of MRI data. H.J.: development and preparation of phantoms; acquisition and processing of MRI data. E.F.-A.: development of tumor model, interpretation of tumor data. D.B.: preparation of tumor samples and acquisition of MRI data. D.T.: development of theory, TopSpin data acquisition code, and Matlab data inversion code; simulations; drafting and revising the manuscript. All authors contributed to the final version of the manuscript.

Omar Narvaez: Conceptualization (equal); Funding acquisition (equal); Investigation (equal); Methodology (equal); Resources (equal); Software (equal); Supervision (equal); Visualization (equal); Writing – original draft (equal); Writing – review & editing (equal). **Maxime Yon**: Investigation (equal); Methodology (equal); Software (equal); Writing – review & editing (equal). **Hong Jiang**: Investigation (equal); Methodology (equal); Software (equal); Writing – review & editing (equal). **Diana Bernin**: Investigation (equal); Methodology (equal); Writing – review & editing (equal). **Eva Forssell-Aronsson**: Investigation (equal); Methodology (equal); Resources (equal); Writing – review & editing (equal). **Alejandra Sierra**: Investigation (equal); Methodology (equal); Resources (equal); Writing – review & editing (equal). **Daniel Topgaard**: Conceptualization (equal); Funding acquisition (equal); Investigation (equal); Methodology (equal); Resources (equal); Software (equal); Supervision (equal); Visualization (equal); Writing – original draft (equal); Writing – review & editing (equal).

DATA AVAILABILITY

Upon manuscript acceptance, data and code will be made available at https://github.com/daniel-topgaard/.

REFERENCES

[1] W. S. Price, *NMR Studies of Translational Motion* (Cambridge University Press, Cambridge, 2009).

[2] P. T. Callaghan, *Translational Dynamics and Magnetic Resonance* (Oxford University Press, Oxford, 2011).

[3] C. Beaulieu, NMR Biomed. **15**, 435 (2002).

[4] D. Topgaard, in *Advanced Diffusion Encoding Methods in MRI*, edited by D. Topgaard (Royal Society of Chemistry, Cambridge, 2020), p. 1.

[5] D. Le Bihan *et al.*, Radiology **161**, 401 (1986).

[6] H. L. Lutsep *et al.*, Ann. Neurol. **41**, 574 (1997).

[7] J. O. Barentsz *et al.*, Eur. Urol. **69**, 41 (2016).

[8] A. Reymbaut, in *Advanced Diffusion Encoding Methods in MRI*, edited by D. Topgaard (Royal Society of Chemistry, Cambridge, 2020), p. 68.

[9] M. Aggarwal, in *Advanced Diffusion Encoding Methods in MRI*, edited by D. Topgaard (Royal Society of Chemistry, Cambridge, 2020), p. 103.

[10] F. B. Laun and A. Wetscherek, in *Advanced Diffusion Encoding Methods in MRI*, edited by D. Topgaard (Royal Society of Chemistry, Cambridge, 2020), p. 123.

[11] M. Schillmaier, A. Kaika, and F. Schilling, in *Advanced Diffusion Encoding Methods in MRI*, edited by D. Topgaard (Royal Society of Chemistry, Cambridge, 2020), p. 154.

[12] A. Reymbaut *et al.*, in *Advanced Diffusion Encoding Methods in MRI*, edited by D. Topgaard (Royal Society of Chemistry, Cambridge, 2020), p. 406.

[13] D. S. Novikov, V. G. Kiselev, and S. N. Jespersen, Magn. Reson. Med. **79**, 3172 (2018).

[14] D. C. Alexander *et al.*, NMR Biomed. **32**, e3841 (2019).

[15] A. Einstein, Ann. Phys. **17**, 549 (1905).

[16] D. E. Woessner, J. Phys. Chem. **67**, 1365 (1963).

[17] G. E. Uhlenbeck and L. C. Ornstein, Phys. Rev. **36**, 823 (1930).

[18] J. Stepišnik, Physica B **104**, 305 (1981).

[19] P. T. Callaghan and J. Stepišnik, J. Magn. Reson., Ser. A **117**, 118 (1995).

[20] P. T. Callaghan and J. Stepišnik, in *Adv. Magnetic Optical Resonance*, edited by W. S. Warren (Academic Press, Inc., San Diego, 1996), p. 325.

[21] E. C. Parsons, Jr., M. D. Does, and J. C. Gore, Magn. Reson. Med. **55**, 75 (2006).

[22] H. Lundell and S. Lasič, in *Advanced Diffusion Encoding Methods in MRI*, edited by D. Topgaard (Royal Society of Chemistry, Cambridge, 2020), p. 12.

[23] P. Tetreault *et al.*, Neuroimage **210**, 116533 (2020).

[24] A. Arbabi *et al.*, Magn. Reson. Med. **83**, 2197 (2020).

[25] J. Xu *et al.*, Magn. Reson. Med. **83**, 2002 (2020).

[26] F. Hennel, E. S. Michael, and K. P. Pruessmann, NMR Biomed. **34**, e4434 (2021).

03 September 2024 10:04:04

[27]E. T. Tan *et al.*, Magn. Reson. Med. **84**, 950 (2020).

[28]T. Maekawa *et al.*, Magn. Reson. Imaging **72**, 34 (2020).

[29]J. Xu *et al.*, Magn. Reson. Med. **85**, 748 (2021).

[30]J. Stepišnik, J. Magn. Reson. **131**, 339 (1998).

[31]J. Stepišnik, Physica B **183**, 343 (1993).

[32]D. S. Novikov *et al.*, Proc. Natl. Acad. Sci. U. S. A. **111**, 5088 (2014).

[33]E. Fieremans *et al.*, Neuroimage **129**, 414 (2016).

[34]H.-H. Lee *et al.*, Neuroimage **222**, 117054 (2020).

[35]S. Portnoy *et al.*, Magn. Reson. Med. **69**, 1131 (2013).

[36]P. J. Basser, J. Mattiello, and D. Le Bihan, J. Magn. Reson., Ser. B **103**, 247 (1994).

[37]H. Jiang, L. Svenningsson, and D. Topgaard, Magn. Reson. **4**, 73 (2023).

[38]S. Eriksson *et al.*, J. Chem. Phys. **142**, 104201 (2015).

[39]D. Topgaard, in *Diffusion NMR of Confined Systems: Fluid Transport in Porous Solids and Heterogeneous Materials*, edited by R. Valiullin (Royal Society of Chemistry, Cambridge, 2016), p. 226.

[40]D. Topgaard, J. Magn. Reson. **275**, 98 (2017).

[41]A. L. Alexander *et al.*, Magn. Reson. Med. **45**, 770 (2001).

[42]A. Ramirez-Manzanares *et al.*, IEEE Trans. Med. Imaging **26**, 1091 (2007).

[43]O. Pasternak *et al.*, Magn. Reson. Med. **62**, 717 (2009).

[44]H. Zhang *et al.*, Neuroimage **61**, 1000 (2012).

[45]N. S. White *et al.*, Hum. Brain Mapp. **34**, 327 (2013).

[46]B. Scherrer *et al.*, Magn. Reson. Med. **76**, 963 (2016).

[47]P. J. Basser and S. Pajevic, IEEE Trans. Med. Imaging **22**, 785 (2003).

[48]B. Jian *et al.*, Neuroimage **37**, 164 (2007).

[49]A. D. Leow *et al.*, Magn. Reson. Med. **61**, 205 (2009).

[50]K. N. Magdoom *et al.*, Sci. Rep. **11**, 2766 (2021).

[51]Y. Song *et al.*, Front. Phys. **10**, 813475 (2022).

[52]E. O. Stejskal and J. E. Tanner, J. Chem. Phys. **42**, 288 (1965).

[53]D. G. Cory, A. N. Garroway, and J. B. Miller, Polymer Prepr. **31**, 149 (1990).

[54]S. Mori and P. C. M. van Zijl, Magn. Reson. Med. **33**, 41 (1995).

[55]C.-F. Westin *et al.*, in *Medical Image Computing and Computer-Assisted Intervention – MICCAI 2014* (Springer, Cham, 2014), Vol. 17, p. 209.

[56]C.-F. Westin *et al.*, Neuroimage **135**, 345 (2016).

[57]J. P. de Almeida Martins and D. Topgaard, Phys. Rev. Lett. **116**, 087601 (2016).

[58]D. Topgaard, NMR Biomed. **32**, e4066 (2019).

[59]M. Yon *et al.*, NMR Biomed. **33**, e4355 (2020).

[60]I. Daimiel Naranjo *et al.*, Cancers **13**, 1606 (2021).

[61]J. P. de Almeida Martins and D. Topgaard, Sci. Rep. **8**, 2488 (2018).

[62]A. Reymbaut *et al.*, NMR Biomed. **33**, e4267 (2020).

[63]D. Topgaard, J. Magn. Reson. **306**, 150 (2019).

[64]A. Caprihan and E. Fukushima, Phys. Rep. **198**, 195 (1990).

[65]E. C. Parsons, M. D. Does, and J. C. Gore, Magn. Reson. Imaging **21**, 279 (2003).

[66]H. Lundell, C. K. Sønderby, and T. B. Dyrby, Magn. Reson. Med. **73**, 1171 (2015).

[67]S. Eriksson, S. Lasič, and D. Topgaard, J. Magn. Reson. **226**, 13 (2013).

[68]D. Topgaard, Phys. Chem. Chem. Phys. **18**, 8545 (2016).

[69]C. Pierpaoli *et al.*, Radiology **201**, 637 (1996).

[70]J. H. Jensen *et al.*, Magn. Reson. Med. **53**, 1432 (2005).

[71]S. Lasič *et al.*, Front. Phys. **2**, 11 (2014).

[72]F. Szczepankiewicz *et al.*, Neuroimage **104**, 241 (2015).

[73]D. Boito, C. Yolcu, and E. Özarslan, Front. Phys. **10**, 830274 (2022).

[74]C. Yolcu *et al.*, Phys. Rev. E **93**, 052602 (2016).

[75]O. Narvaez *et al.*, arXiv:2111.07827 (2021).

[76]A. Romiani *et al.*, BMC Cancer **21**, 950 (2021).

[77]K. W. Andersen *et al.*, Brain Commun. **2**, fcaa077 (2020).

[78]B. Lampinen *et al.*, Epilepsia **61**, 1701 (2020).

[79]M. Nilsson *et al.*, Magn. Reson. Med. **83**, 608 (2020).

[80]S. Li *et al.*, Eur. Radiol. **31**, 8197 (2021).

[81]N. J. J. Arezza, D. H. Y. Tse, and C. A. Baron, Magn. Reson. Imaging **80**, 132 (2021).

[82]J. Stepišnik *et al.*, J. Magn. Reson. **182**, 195 (2006).

[83]D. S. Novikov *et al.*, Nat. Phys. **7**, 508 (2011).

[84]C. H. Neuman, J. Chem. Phys. **60**, 4508 (1974).

[85]P. B. Kingsley, Concepts Magn. Reson., Part A **28A**, 123 (2006).

[86]C. Ligneul and J. Valette, NMR Biomed. **30**, e3671 (2017).

[87]U. Haeberlen, *High Resolution NMR in Solids Selective Averaging*, *Advances in Magnetic Resonance* (Academic Press, New York, 1976).

[88]M. Prange and Y. Q. Song, J. Magn. Reson. **196**, 54 (2009).

[89]J. P. de Almeida Martins *et al.*, Magn. Reson. **1**, 27 (2020).

[90]J. P. de Almeida Martins *et al.*, Hum. Brain Mapp. **42**, 310 (2021).

[91]A. Reymbaut *et al.*, Magn. Reson. Med. **85**, 2815 (2021).

[92]J. Martin *et al.*, Neuroimage **245**, 118753 (2021).

[93]K. P. Whittal, M. J. Bronskill, and R. M. Henkelman, J. Magn. Reson. **95**, 221 (1991).

[94]T. E. Conturo *et al.*, Magn. Reson. Med. **35**, 399 (1996).

[95]M. Aggarwal *et al.*, Magn. Reson. Med. **67**, 98 (2012).

[96]K. D. Harkins *et al.*, Neuroimage **227**, 117619 (2021).

[97]M. Lawrenz, M. A. Koch, and J. Finsterbusch, J. Magn. Reson. **202**, 43 (2010).

[98]N. Shemesh *et al.*, Magn. Reson. Med. **75**, 82 (2016).

[99]S. N. Jespersen *et al.*, NMR Biomed. **26**, 1647 (2013).

[100]J. Xu *et al.*, NMR Biomed. **29**, 400 (2016).

[101]C. Pierpaoli and P. J. Basser, Magn. Reson. Med. **36**, 893 (1996).

[102]R. N. Henriques, S. N. Jespersen, and N. Shemesh, Neuroimage **211**, 116605 (2020).

[103]M. Aggarwal, M. D. Smith, and P. A. Calabresi, Magn. Reson. Med. **84**, 1564 (2020).

[104]M. Bak and N. C. Nielsen, J. Magn. Reson. **125**, 132 (1997).

[105]C. Malmborg *et al.*, J. Magn. Reson. **180**, 280 (2006).

[106]L. Wadsö *et al.*, Eur. J. Pharm. Biopharm. **72**, 99 (2009).

[107]N.-O. Persson *et al.*, J. Colloid Interface Sci. **53**, 461 (1975).

[108]M. Nilsson *et al.*, Proc. Int. Soc. Mag. Reson. Med. **26**, 5355 (2018).

[109]R. Mills, J. Phys. Chem. **77**, 685 (1973).

[110]I. Åslund *et al.*, J. Magn. Reson. **200**, 291 (2009).

[111]U. Balucani, J. P. Brodholt, and R. Vallauri, J. Phys.: Condens. Matter **8**, 6139 (1996).

[112]B. J. Claiborne, D. G. Amaral, and W. M. Cowan, J. Comp. Neurol. **302**, 206 (1990).

[113]B. Balinov *et al.*, J. Magn. Reson., Ser. A **104**, 17 (1993).

[114]J. Stepišnik, Physica B **270**, 110 (1999).

[115]P. T. Callaghan *et al.*, Nature **351**, 467 (1991).

[116]B. Balinov, O. Söderman, and J. C. Ravey, J. Phys. Chem. **98**, 393 (1994).

[117]S. J. Gibbs, J. Magn. Reson. **124**, 223 (1997).

[118]P. W. Kuchel, A. Coy, and P. Stilbs, Magn. Reson. Med. **37**, 637 (1997).

[119]M. M. Milne and M. S. Conradi, J. Magn. Reson. **197**, 87 (2009).